Microscale diffusion-mechanics model for a polymer-based solid-state battery cathode

Leyla Sultanova[a], Łukasz Figiel[a,b,*]

[a] *International Institute for Nanocomposites Manufacturing (IINM), WMG, University of Warwick, CV4 7AL, UK*
[b] *Warwick Centre for Predictive Modelling (WCPM), University of Warwick, CV4 7AL, UK*

A B S T R A C T

A non-linear microscale diffusion-mechanics model combining mass transport and linear momentum balance equations, with elasto-viscoplastic polymer constitutive law and interfacial traction-separation law is proposed to provide a new insight into the effects of viscoplasticity and interfacial damage on the in situ diffusive-mechanical behaviour of a polymer-based cathode for a solid-state battery (SSB). Diffusion and mechanics are coupled through two mechanisms: (1) active particle (AP) volumetric change dependence on Li concentration, and (2) interfacial flux dependence on mechanical opening. The model is resolved for a simple cathode microstructure using an axisymmetric unit cell concept, and integrated with the non-linear finite-element solver ABAQUS with the help of its user subroutines (UMAT and UINTER). Finite-element simulations reveal that plastic deformations of the polymer due to volumetric changes of the AP reduce the value of the interfacial opening displacement, which is desirable for maintaining interfacial flux. The results also demonstrate that slower battery charging rates may lead to a softer polymer response, and thus a smaller interfacial gap. Moreover, a comparison between the linear elastic and current elasto-viscoplastic models for the polymer electrolyte shows that even 5% volumetric shrinkage of the AP leads to an overprediction of the interfacial opening with the linear elastic material law, which limits its validity in modelling polymer-based SSBs.

1. Introduction

Rechargeable Li-ion batteries (LIBs) are the most widely used energy storage systems due to their high specific energy storage and power density. Their high energy efficiency provides promising opportunities for the two large potential markets: (1) electrification in automotive industry (power batteries), and (2) development of large-scale stationary batteries that store energy from natural resources such as sunlight and wind (storage batteries), see e.g. [1].

In a conventional LIB with liquid electrolyte electrodes comprise of active particles (APs), which are embedded into a matrix typically consisting of a conducting material and binder, and liquid electrolyte that fills electrodes' pores. Charge and discharge processes in LIBs are based on Li insertion into or extraction from electrodes' APs, which results in cyclic volumetric changes due to swelling and shrinkage of APs. The resulting strains may have adverse effects on the structural integrity and electrochemical performance of LIBs. Therefore, the mechanical degradation of batteries caused by such cyclic deformation has attracted tremendous scientific interest over the recent years, see e.g. [2,3] for an overview of stress-related issues and degradation

mechanisms in various electrode materials, and [4] for a comprehensive review on electro-chemo-mechanical modelling of LIBs.

Fracture and damage of APs and electrodes have been the main focus of research into degradation mechanisms in LIBs with liquid electrolytes, see e.g. [5–8], or more recent [9], where an intergranular cracking within a positive electrode represented as a poly-crystalline medium was studied using a small-strain non-linear chemo-mechanical framework. Interfacial debonding is another crucial failure mechanism that can lead to a disruption of conducting paths and decreased cell performance. However, it appears to be less explored. Among few studies is [10] where an interfacial debonding between NMC particles and conductive matrix was modelled by means of electro-chemo-mechanical theory and a comprehensive 3D microstructure-based approach aiming at establishing a relationship between interfacial damage and impedance of electrical transport and surface charge transfer.

In recent years, solid state batteries (SSBs) with solid electrolytes (SEs) have been intensively studied as a potential replacement of conventional LIBs, as they present some safety advantages such as reduced flammability and risk of leakage. One of the proposed electrodes architecture for SSB is a composition of active materials and SE, see

---

[11,12], so that APs appear to be embedded directly into SE, increasing Li transport capabilities of a cell to a level comparable to conventional LIBs with liquid electrolytes. However, in this case SSBs are even more prone to mechanical degradation during cycling than their liquid electrolytes counterparts due to a more rigid material environment surrounding APs (especially for SEs made of ceramic materials) and a low electrode porosity, which offers a limited possibility to accommodate deformations resulting from repeated volumetric changes of APs. Moreover, once a gap between two material phases is formed, the mass transport across it becomes reduced or blocked, unlike for LIBs with liquid electrolytes, where liquid electrolyte can fill the gaps and help to maintain the mass transport. Therefore, an investigation into light-weight, deformable, and ionically-conductive SEs is still a work-in-progress, where one of the potential candidates is a polymer-based SE, see [13–15]. An example of a SSB coin cell fabricated by sandwiching electrodes and polymer-based SE is reported in [16].

Advances in modelling of SSBs with polymer-based SEs have mainly focused on the electrochemical performance of polymer-based SEs, see e.g. [17], and electro-chemo-mechanical modelling of polymer-based SEs, see [18,19], at the cell level, where the effect of stresses is included *via* pressure. Microscale damage modelling of SSBs was considered in [20], where a simplified cathode material microstructure was studied in 2D addressing the issue of SE fracture. Then, a 1D analytical approach aiming at capturing interfacial mechanical failure between an AP and SE was proposed in [21]. All those modelling studies have assumed linear elastic (LE) constitutive model for the description of mechanical response of material components in SSBs. However, in case of polymer-based SE, lithiation/delithiation cycles may cause it to undergo plasticity, thus, LE approximation will be insufficient. Moreover, SSBs can be charged at different rates sufficient to trigger viscoelastic phenomena in polymer-based SEs. Hence, an accurate description of the mechanical response of polymer-based SEs for SSBs requires formulation and implementation of finite-strain elasto-viscoplastic (EVP) constitutive (material) models, even for relatively small volumetric changes of APs. Therefore, this work proposes a microscale approach that attempts to couple mechanics with diffusion, and incorporates a finite-strain EVP description of polymer-based SE. The approach is then used to investigate the effects of polymer-based SE material non-linearity and strain-rate dependence on the in situ response of a composite electrode, and, in particular, the effects of polymer-based SE elasto-viscoplasticity on interfacial damage and contact loss between AP and polymer-based SE.

The paper starts with the description of the model background followed by its mathematical formulation and details of numerical implementation into a finite-element solver ABAQUS. The results showing the effects of polymer-based SE viscoplasticity on the AP-SE interfacial behaviour are then discussed in detail. Notation and the list of abbreviations used in the paper are given in Appendix.

2. Model concept and assumptions

A typical SSB cell consists of positive and negative electrodes, SE and current collectors, see Fig. 1(a). Commonly, the material of a positive electrode (cathode) is highly heterogeneous and, therefore, prone to microstructural degradation such as interfacial damage, especially upon the very first electrochemical cycle. Thus, cathode is the main focus in the present study. SE, in turn, is considered to be polymer-based, therefore, in what follows, abbreviation SE refers to polymer-based SE. Here it is assumed that APs are embedded into an ionically-conducting solid matrix made of the same material as SE, see Fig. 1(b). This implies a possible future SSB cell design that may avoid a distinct interface between SE and the cathode. However, an interfacial damage

can still occur between APs and SE as a result of particle shrinkage and swelling, and may be significantly affected by the EVP response of SE.

One of the main approaches to modelling of materials with microstructural heterogeneity is the computational homogenisation concept, see [22]. The key components of the scheme are formulation of a microstructural boundary value problem (BVP) for a representative volume element (RVE), and coupling between micro and macro levels based on averaging theorems. Specific examples of this approach can be found e.g. in [23] for mechanical problem, in [24] for heat conduction, and in [25] for thermo-mechanical analysis. A multiphysics computational homogenisation concept was also formulated for conventional LIBs with liquid electrolytes in [26], and for the ionic transport in LIBs [27]. In this paper, however, the interest is on the in situ response of the cathode at the microscale, rather than on the overall response of the SSB cell. Therefore, a simple microlevel unit cell with just one AP embedded into SE is used. Such a formulation is naturally symmetric, thus, running a full 3D simulation is computationally inefficient compared to available 2D assumptions i.e. plane stress, plane strain, or axisymmetric. Among these the latter is an exact 3D representation of a spherical AP, and in the plane perpendicular to the x_2 direction can be considered as an approximation of the hexagonal arrangement of particles, see e.g. [28]. Hence, for the sake of computational cost reduction, the problem is reduced to an axisymmetric one, see Fig. 1(c). It is also noteworthy to mention that this is a significant geometrical simplification of the complex cathode microstructure. Nevertheless, it is believed that this simplified approach can still provide a fresh insight into the effects of SE viscoplasticity on the interfacial contact loss at the microscale, before more complex microstructures accounting for multiple APs and porosity are considered.

In general, electro-chemo-mechanical process takes place in the cathode including the kinetics of electron and ion transports together with the deformation kinematics. The evolution of mechanical field is driven by the diffusion and the arising mechanical stresses can affect the ions transport and charge transfer reactions, which, in turn, affect the diffusion. Since the mechanics and diffusion have a direct impact on each other, the focus of this study is on these two fields and the coupling between them. The mathematical formulation of the problem assumes that Li transport in the AP and SE can be described as a Fickean diffusion. The electric field as well as the explicit chemical reaction are not considered in the model, therefore, Li refers to both Li and Li-ions throughout the paper. Li transport from/into the AP, and from/into the SE towards/away from the anode (negative electrode) is captured by means of phenomenological interfacial and boundary conditions. Volumetric changes of the AP are considered to be dependent on Li concentration. Further, positive electrodes are frequently assembled in the lithiated state, see [20], and, therefore, the cathode's AP is assumed to be shrinking during the very first charge cycle as Li is extracted from it. Then, since no experimental evidence exists on the interfacial mechanical interactions across AP-SE matrix interfaces, it is presumed that some degree of chemical and physical bonding is possible at the interface. As a result, an exponential traction-separation law is implemented in the normal direction. The rigid body rotation of the AP is constrained by axisymmetric setup and shear sliding is negligibly small compared to the opening in normal direction upon shrinkage (swelling) of just one AP, hence, frictionless sliding is implied in shear. It is worth noting that for complex microstructures with multiple APs, their rigid body rotations should be prevented and the shear interfacial sliding is expected to be more pronounced due to APs interaction, thus, non-zero shear interactions should be considered. There is also a lack of experimental evidence on the effect of contact loss on the Li transport across the AP-SE interface, therefore, some hypothetical interfacial transport laws are proposed relating corresponding flux and opening
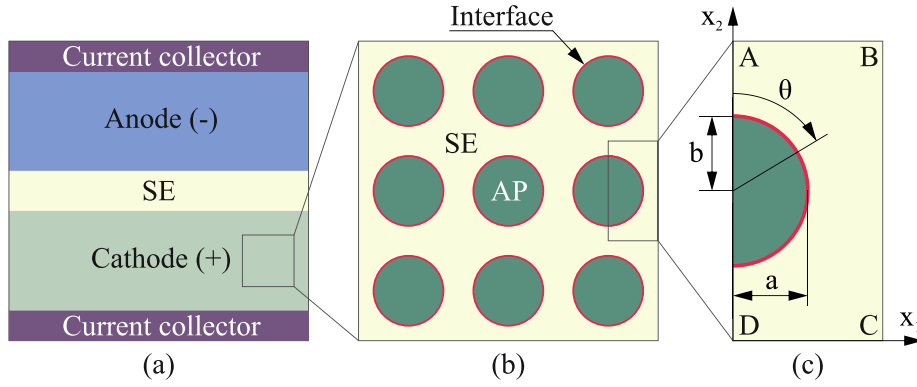
Fig. 1. (a) SSB cell design concept; (b) cathode microstructure; (c) axisymmetric unit cell.

displacement.

The AP is considered to have an idealised spherical shape (a case with a small deviation from this is also addressed). Its mechanical behaviour is assumed to be LE and isotropic – a simplification of a real response of a cathode's AP that may be a polycrystalline material system, behave non-linearly (including irreversible strain and damage), and experience anisotropic swelling/shrinkage, see e.g. [29]. The SE is assumed to be made of a glassy-like polymer which is expected to have a higher ionic conductivity than its semi-crystalline counterpart. An EVP constitutive model is employed in order to capture its non-linear strain-rate dependent response. A drawback of a glassy polymer, however, may be its low thermal stability once the operational temperature of the battery is near or above its glass transition temperature. Nevertheless, thermal effects are beyond the scope of the present paper.

3. Main equations

The equations governing mechanics and diffusion in the proposed computational model are summarised below. They include balance equations, constitutive relations, initial, boundary and interfacial conditions. Mechanics-diffusion coupling is also discussed.

3.1. Mechanics

3.1.1. Equilibrium and bulk material laws

The mechanical process is governed by the balance of linear momentum neglecting mechanical body forces and inertia effects

$$\overrightarrow{\nabla}\cdot\boldsymbol{\sigma} = 0, \tag{1}$$

where $\boldsymbol{\sigma}$ is Cauchy stress tensor.

The equilibrium equation above is complemented by the constitutive (material) laws for the AP and SE. In particular, a standard LE constitutive law is used for the AP which is described by two elastic constants (i.e. Young's modulus E and Poisson's ratio ν).

Then, a phenomenological EVP material relation is employed for glassy polymer SE, following the approach of e.g. [30–32]. The relation assumes two main physical processes contributing to the mechanical response of the polymer: *Process 1* (*P1*) intra- and inter-molecular interactions determining viscoelastic behaviour at small strains and plasticity, and *Process 2* (*P2*) entangled network that controls the strain hardening response. As a result, Cauchy stress tensor can be decomposed as

$$\boldsymbol{\sigma} = \boldsymbol{\sigma}_s^d + \boldsymbol{\sigma}_h^d + \boldsymbol{\sigma}_v, \tag{2}$$

where the deviatoric stress governing the *P1* (see above) is given by

$$\boldsymbol{\sigma}_s^d = G_s J_e^{-1} \bar{\boldsymbol{B}}_e^d, \tag{3}$$

while the deviatoric stress capturing the network behaviour (*P2* above) is as follows

$$\boldsymbol{\sigma}_h^d = G_h J_e^{-1} \bar{\boldsymbol{B}}^d. \tag{4}$$

The two terms are accompanied by the contribution from the hydrostatic (volumetric) stress

$$\boldsymbol{\sigma}_v = K(1 - J_e^{-1})\boldsymbol{I}. \tag{5}$$

In the above, superscript "d" denotes deviatoric part of a tensor, K, G_s and G_h are the bulk, shear and strain hardening moduli, respectively, $\boldsymbol{I}$ is the second-order identity tensor. Moreover, the total and elastic isochoric left Cauchy-Green tensors, $\bar{\boldsymbol{B}}$ and $\bar{\boldsymbol{B}}_e$, respectively, are given by

$$\bar{\boldsymbol{B}} = (J)^{-\frac{2}{3}}\boldsymbol{F}\cdot\boldsymbol{F}^T, \qquad \bar{\boldsymbol{B}}_e = (J_e)^{-\frac{2}{3}}\boldsymbol{F}_e\cdot\boldsymbol{F}_e^T, \tag{6}$$

where $\boldsymbol{F}$ denotes the total deformation gradient tensor, and $\boldsymbol{F}_e$ stands for its elastic part (following the multiplicative decomposition of the deformation gradient into its elastic and plastic parts, i.e. $\boldsymbol{F} = \boldsymbol{F}_e\cdot\boldsymbol{F}_p$, see [33]), $J = \det(\boldsymbol{F})$ and $J_e = \det(\boldsymbol{F}_e)$ are the total and elastic volume ratios, respectively.

A non-Newtonian flow rule is adopted to relate the plastic part of the deformation rate tensor to the stress driving the *P1* process as

$$\boldsymbol{D}_p = \frac{\boldsymbol{\sigma}_s^d}{2\eta} \tag{7}$$

where η denotes viscosity given by a power law

$$\eta = \tau_0 \sigma_0 \left(\frac{\sigma_0}{\bar{\sigma}_s}\right)^q, \qquad \bar{\sigma}_s = \sqrt{\frac{3}{2}\boldsymbol{\sigma}_s^d:\boldsymbol{\sigma}_s^d}, \tag{8}$$

where $\bar{\sigma}_s$ is the equivalent deviatoric stress driving the *P1* process, τ_0, and q are material constants and parameter σ_0 is introduced to avoid using dimentional units in power q. It is worth mentioning that plastic deformation is assumed to be isochoric, i.e. $\det(\boldsymbol{F}_p) = 1$ ($\boldsymbol{F}_p$ is the plastic part of the deformation gradient $\boldsymbol{F}$), and spin-free, i.e. $\boldsymbol{W}_p = \boldsymbol{0}$. Thus, $J = J_e$ and the plastic part of the velocity gradient is given by $\boldsymbol{L}_p = \boldsymbol{D}_p$.

3.1.2. AP-SE interface

A traction-separation law between normal interfacial opening displacement χ and traction t is implied at the AP-SE interface. In particular, a simple universal binding law ([34]) is adopted as

$$t = t_0 \frac{\chi}{\chi_0}\exp\left(1 - \frac{\chi}{\chi_0}\right), \tag{9}$$

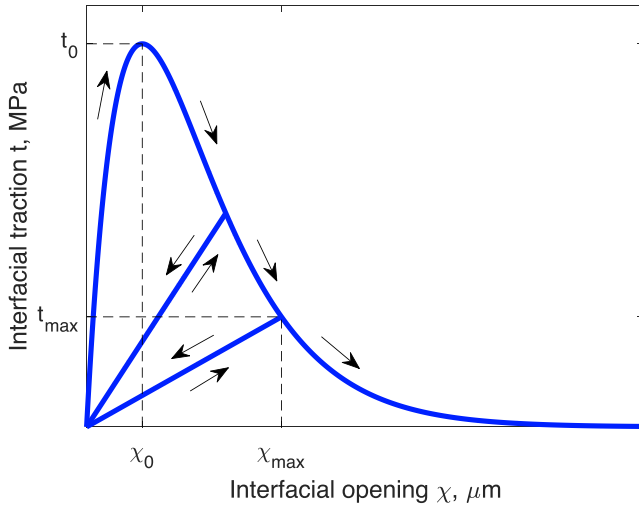where t_0 is the maximum effective traction with χ_0 being its

Fig. 2. Traction-separation law with loading-unloading paths.

corresponding separation, see Fig. 2. Following [35], linear unloading to the origin is assumed such as

$$t = \frac{t_{max}}{\chi_{max}} \chi, \tag{10}$$

where χ_{max} is the maximum opening that has ever been achieved during previous loading and t_{max} is the corresponding cohesive traction.

3.1.3. Mechanical boundary conditions

As mentioned above, axisymmetric configuration is considered, see Fig. 1(c). Hence, the advantage of the problem symmetry (in geometry) with respect to axis x_1 is taken, i.e. $u_1 = 0$ is set on the symmetry line (boundary AD in the Figure). Node D is also fixed in x_2 direction, i.e. $u_2 = 0$, to suppress rigid body translation. Here, u_1 and u_2 represent horizontal and vertical displacement vector components along axes x_1 and x_2, respectively. Furthermore, in order to account for the unit cell periodicity within the cathode, periodic boundary conditions are applied to its boundaries such as

$$u_2^{AB} - u_2^{DC} = u_2^{A} - u_2^{D} \tag{11}$$

and

$$u_1^{BC} = u_1^{B}, \tag{12}$$

where u_2^{AB}, u_2^{DC}, u_1^{BC}, u_2^{A}, u_2^{D} and u_1^{B} are the corresponding vertical and horizontal displacement vector components of the upper, lower and right hand side boundaries of the unit cell (lines AB, DC and BC Fig. 1(c)) and the unit cell nodes (A, D, B). It is worth noting that since the interest of the paper is on the in situ response of the cathode at the microscale level rather than on the overall response of the SSB cell, the macroscopic deformation of the cathode is not taken into consideration.

3.2. Diffusion

3.2.1. Bulk diffusion

As it was pointed out in [36], a steady-state mass transport hypothesis at the microscale level adopted for heat conduction in [24,25], is not satisfied for the battery problem. Therefore, the transient mass balance equation is used instead to describe the diffusion process

$$\frac{\partial c}{\partial t} = -\vec{\nabla} \cdot \vec{j}, \tag{13}$$

where c is the Li molar concentration and $\vec{j}$ indicates the mass flux.

The flux in both AP and SE is expressed as Fick's 1st law

$$\vec{j} = -D \vec{\nabla} c, \tag{14}$$

with D indicating the bulk diffusion constant. This simplified description was exploited in e.g. [37] for electrochemical modelling of a microbattery with liquid electrolyte. It is worth noting that the expression for the flux in the electrolyte can also contain the term associated with migration of ions along with the diffusive term introduced in the right-hand side of (14), see e.g. [10]. Similar approach was suggested for modelling of the flux in SE, in particular, Nernst-Planck's equation was adopted in [17]. Moreover, following [38,39], the modification of Nernst-Planck's equation was proposed in [18,19] in order to introduce the effect of mechanical stresses in solid material. The latter can also be taken into account in the active material, see e.g. [10].

A concentration range corresponding to the cell capacity can be defined using stoichiometry

$$x = \frac{c_{av}^{AP}}{c_{max}^{AP}}, \tag{15}$$

see e.g. [40], where c_{av}^{AP} represents the average Li concentration in the AP at a given time and c_{max}^{AP} indicates the maximum Li concentration. During cycling a cathode does not fully delithiate/lithiate, therefore, stoichiometry corresponding to 100% and 0% state of charge (SOC) is not equal to 0 and 1. Instead, it ranges between values $x_{100\%}$ and $x_{0\%}$, which can be calculated using e.g. Open Circuit Voltage (OCV) curve, see [40]. The corresponding concentrations are denoted by $c_{100\%}^{AP}$ and $c_{0\%}^{AP}$ and can be derived using calculated stoichiometries $x_{100\%}$ and $x_{0\%}$ and maximum Li concentration c_{max}^{AP}, see Subsection 4.1. As cathodes are assembled in the lithiated state, a fully discharged battery is assumed to be in a stress-free state. Therefore, $c_{0\%}^{AP}$ is considered as an initial condition for the AP (note, that $c_{0\%}^{AP}$ is used here instead of c_{max}^{AP} for simplicity). The matrix, in turn, is set to possess some residual Li concentration c_{res}^{SE}.

3.2.2. Diffusion across the interface

Interfacial kinetics is typically modelled *via* classical Butler-Volmer equation, see [41], using the concept of a surface overpotential. Since the electric field is not considered in the present study, in order to model Li transport from/into the AP the following phenomenological interfacial condition is introduced

$$\vec{j}_{int} \cdot \vec{n}_{int} = D_{int}(c_{int}^{AP} - c_{ref}^{AP})c_{int}^{SE}, \tag{16}$$

where $\vec{n}_{int}$ is the AP outward normal vector in the current (deformed) configuration, D_{int} stands for the interfacial diffusivity, c_{int}^{AP} and c_{int}^{SE} are Li concentrations at the interface of the AP and SE at a given time, i.e. the values of c_{int}^{AP} and c_{int}^{SE} vary with time during charge and discharge. Reference AP concentration c_{ref}^{AP} is a constant which drives the interfacial flux. It is set as $c_{ref}^{AP} = c_{100\%}^{AP}$ and $c_{ref}^{AP} = c_{0\%}^{AP}$ for charge and discharge processes, respectively, i.e. during charge/discharge the flux from/into the AP is present as long as c_{int}^{AP} has not reached the value of $c_{100\%}^{AP}/c_{0\%}^{AP}$.

3.2.3. Boundary conditions for diffusion

In order to model Li flux from/into the SE towards/away from the anode, the phenomenological boundary condition is applied at the upper boundary of the unit cell (line AB in Fig. 1(c)) as follows

$$\vec{j}_b \cdot \vec{n}_b = D_b(c_b^{SE} - c_{res}^{SE}). \tag{17}$$

Here, $\vec{n}_b$ is the boundary outward normal vector in the current configuration, D_b denotes the boundary diffusivity and c_b^{SE} indicates SE boundary Li concentration at a given time, i.e. it varies with time during charge and discharge. As it was discussed above, initially, Li
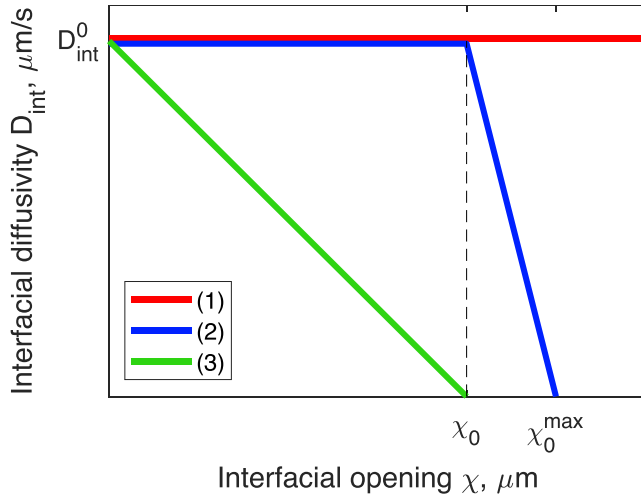
Fig. 3. Variation of interfacial diffusivity as a function of mechanical opening.

Table 1
Parameter set for the simulations.

Symbol	Description	Value	Ref
	AP material parameters – NMC		
–	Diameter	10 μm	[44,46,40]
–	Volume change	5 %	[44,46,40]
E^{AP}	Young's modulus	130 GPa	[44,46]
ν^{AP}	Poisson's ratio	0.25	[49]
$c_{100\%}^{AP}$	Li concentration at 100% SOC	13 fmol/μm³	[40]
$c_{0\%}^{AP}$	Li concentration at 0% SOC	45.8 fmol/μm³	[40]
D^{AP}	Li diffusion coefficient	0.025 μm²/s	[51,43]
	SE material parameters – PEO based		
E^{SE}	Young's modulus	100 MPa	Fitted
ν^{SE}	Poisson's ratio	0.24	[42]
q	Power law parameter	3	Fitted
τ_0	Relaxation time	100 s	Fitted
σ_0	–	2 MPa	Fitted
G_s/G_h	Shear moduli ratio	7	Fitted
D^{SE}	Li diffusion coefficient	3 μm²/s	[54]
c_{res}^{SE}	Residual Li concentration	1 fmol/μm³	[10,40]
	Interfacial and boundary parameters, half-cycle duration, unit cell size		
t_0	Maximum interfacial traction	0.5 (stiff), 0.2 (soft) MPa	Assumed
χ_0	Reference opening	0.04 μm	Assumed
χ_0^{max}	Reference maximum opening	0.042 μm	Assumed
D_{int}^0	Initial interfacial diffusivity	0.025 (5C), 0.005 (1C), 0.001 (C/5) μm/s	Assumed
D_b	Boundary diffusivity	3 μm/s	Assumed
τ	Half-cycle duration	0.2 (5C), 1 (1C), 5 (C/5) h	[10]
–	Unit cell size	10 μm by 20 μm (benchmark), 6.5 μm by 13 μm, 5.5 μm by 11 μm	Assumed

concentration in the SE is set to be equal to c_{res}^{SE}, therefore, $c_b^{SE} = c_{res}^{SE}$. During the first charge the flux from the AP causes the increase in Li concentration in the SE leading to the value of c_b^{SE} becoming greater than c_{res}^{SE} which results in the boundary flux from the SE towards negative electrode. Similar procedure takes place in the reverse process. Note, that the residual Li concentration in the SE during both charge and discharge processes is considered to be equal to the initial one, i.e. c_{res}^{SE} is constant. Moreover, it is assumed that the Li transport towards/away from the anode happens only in a vertical direction, therefore, the remaining boundaries of the unit cell (lines CD, AD, BC on Fig. 1(c)) are considered to be flux free, i.e. $\vec{j}_b \cdot \vec{n}_b = 0$.

3.3. Mechanics-diffusion coupling

Coupling between mechanics and diffusion is implemented through two mechanisms. The first one is based on Vegard's law, see e.g. [9], i.e. strain tensor induced by AP's delithiation/lithiation, ε_{Li}, is assumed to be proportional to Li concentration in the AP at a given time, c^{AP}, such as

$$\varepsilon_{Li} = (c_{0\%}^{AP} - c^{AP})\boldsymbol{\zeta}, \qquad (18)$$

where ζ indicates AP's volume change tensor caused by delithiation/lithiation with $\zeta_{ij} \neq 0$ if $i = j$ and $\zeta_{ij} = 0$ if $i \neq j$. The related volume change is associated with partial molar volume Ω of Li in the material such as $\Omega = \text{tr}(\zeta)$. In this paper, ζ is considered to be isotropic, i.e. $\zeta_{11} = \zeta_{22} = \zeta_{33}$, and therefore, (18) becomes

$$\varepsilon_{Li} = \frac{\Omega}{3}(c_{0\%}^{AP} - c^{AP})\boldsymbol{I}. \qquad (19)$$

The second coupling mechanism implies that the interfacial flux $\vec{j}_{int}$ is dependent on the normal opening displacement χ. In [10], it is enforced by means of the interfacial electrical resistance R_{int} correlated with χ, which causes drop in surface overpotential affecting the Li flux through Butler-Volmer equation. In this study, since an electric field is not considered, it is implemented through variation of interfacial diffusivity D_{int}, i.e. $D_{int} = f(\chi)$, and three possible relations are considered (see Fig. 3): (1) constant D_{int}, (2) constant D_{int} with linear decay upon reaching reference opening χ_0 corresponding to maximum interfacial traction (see Fig. 2), and (3) instant linear decay. The relation (2) is analogical to the ones considered in [7,9].

It is noteworthy to mention that other approaches for mechanics-diffusion coupling can be introduced, e.g. pressure-assisted bulk diffusion discussed in Subsection 3.2.1. The mechanical pressure can also be considered to affect the interfacial flux, see e.g. [38,10] where it is implemented through surface overpotential. Moreover, the material parameters which are assumed to be constant in this paper, can be dependent on deformations and SOC, see e.g. [42,43].

4. Model parameters

The selection of values for model parameters required for simulations is described in this section and additionally summarised in Table 1.

4.1. AP material parameters

Polycrystalline Lithium Nickel Manganese Cobalt Oxide (LiNi$_x$Mn$_y$Co$_z$O$_2$, $x + y + z = 1$) (NMC) is a popular choice for cathode's material in commercial LIBs due to its high capacity, electrochemical stability and cost effectiveness, see e.g. [16], and, thus, is selected here as an active material for the positive electrode. According to SEM images, the cathode made from polycrystalline NMC have secondary particles of nearly spherical shape with an average diameter of about 10 μm, see e.g. [40,44–46]. They are formed from agglomerates of primary particles with a smaller diameter (~300–500 nm), which may be single-crystals or contain grain boundaries. The evolution of NMC a and c lattice parameters, and its unit cell volume during cycling is demonstrated in [45,47,48]. An initial increase of c lattice parameter is followed by a decrease upon charging (NMC delithiation), while lattice

parameter a decreases monotonically. The unit cell volume, in turn, shrinks continuously upon delithiation with a volume change of about 5%. All of these trends are reversible on a subsequent discharge. As a result, the unit cell volume change is anisotropic and non-linear. However, since the AP considered here refers to the polycrystalline NMC secondary particle which is formed by primary particles with random crystal orientations, its volume change is assumed to be isotropic. Moreover, it is also considered to be linear for simplicity, see (19).

Young's modulus of NMC was measured in [44] by targeted and grid nanoindentation and found to be 138.73 ± 18.78 GPa and 123.02 ± 20 GPa, respectively. In [46], targeted nanoindentation was performed at the centre of an NMC$_{532}$ secondary particle resulting in Young's modulus of 142.5 ± 11.3 GPa. Pulse-echo acoustic technique and nanoindentation were carried out in [49] for NMC$_{333}$ hot-pressed pellets with values of 0.25 and 199 ± 12 GPa for Poisson's ratio and Young's modulus, respectively. Therefore, an average value of Young's modulus (E^{AP}) of 130 GPa is chosen for the simulations here, along with an assumed Poisson's ratio (ν^{AP}) of 0.25.

Stoichiometry $x_{100\%}$ and $x_{0\%}$ of NMC$_{811}$ corresponding to maximum and minimum capacity of a cell is determined in [40] as 0.2567 and 0.9072, respectively. The maximum Li concentration c_{max}^{AP} is also calculated as 50,483 mol/m^3, resulting in $c_{100\%}^{AP}$ and $c_{0\%}^{AP}$ being 12,959 and 45,798 mol/m^3, respectively, or 13 and 45.8 fmol/μm^3. Similar value of 48,685 mol/m^3 is reported in [50] for NMC$_{523}$ maximum Li concentration, where it is calculated from theoretical specific capacity and density. Partial molar volume Ω is then calculated using (19) together with chosen values of concentrations and AP volume change.

Value of NMC Li diffusion coefficient varies quite a lot depending on, among other things, characterisation technique used for its evaluation, e.g. Cyclic Voltammetry (CV), Galvanostatic Intermittent Titration Technique (GITT), Electrochemical Impedance Spectroscopy (EIS). A reported range of values is between 10^{-14} and 10^{-8} cm^2/s, see e.g. [43,51], thus, a value of $0.025\,\mu$m^2/s is chosen as Li diffusion coefficient for the AP (D^{AP}) in the simulations.

4.2. SE material parameters

Poly(ethylene oxide) (PEO) with solvated Li salts and ionic liquid (IL) is one of the most extensively studied material candidates for SE in SSBs, e.g. PEO/LiTFSI in [52], PEO/LiTFSI/IL in [16], and PEO/LiClO$_4$

Fig. 4. Simulated stress-strain curves for PEO.

in [42].

Young's modulus (E^{SE}) and viscoplastic parameters (q, τ_0, σ_0, G_s/G_h) required in the constitutive model for the polymer SE are obtained from uniaxial compression stress-strain data for an unmodified PEO carried out at different engineering strain rates. The derived values are 100 MPa, 3, 100 s, 2 MPa and 7, respectively. The determined Young's modulus is close to the value of 70 ± 7 MPa reported in [53]. Poisson's ratio of PEO/LiClO$_4$ is taken as 0.24 from [42]. Total shear modulus $G^{SE} = G_s + G_h$ is obtained using E^{SE}, ν^{SE}, and the standard relation for isotropic solids $G = \frac{E}{2(1+\nu)}$. Cyclic and rate dependent stress-strain curves are plotted in Fig. 4 to demonstrate the behaviour of the constitutive model with the chosen material parameters.

Value of SE Li diffusion coefficient (D^{SE}) of $(0.25 - 3.36)\cdot10^{-8}$ cm^2/s is extracted from [54] where molecular dynamics simulations are performed for PEO with LiPF$_6$ salt, thus, the chosen value for the simulations is $3\,\mu$m^2/s. Finally, following [10,40], residual Li concentration in SE c_{res}^{SE} is set to be 1 fmol/μm^3.

4.3. Unit cell size and active material volume fraction

A volume fraction of the active material in a typical commercial NMC-based cathode is around 70%, see e.g. [40]. However, the benchmark size of the unit cell is chosen as $10\,\mu$m by $20\,\mu$m (lengths of AB and BC on Fig. 1(c)) corresponding to a much lower active material volume fraction of just 8.33% for an axisymmetric unit cell. This allows minimising the effects of APs interactions on the interfacial deformation and, thus, concentrating on local effects of SE plasticity on the interfacial opening. In order to address the impact of the unit cell size (volume fraction of the active material, APs interactions), smaller dimensions of $6.5\,\mu$m by $13\,\mu$m and $5.5\,\mu$m by $11\,\mu$m are also considered which correspond to active material volume fractions of 30.34% and 50.09%, respectively.

4.4. Interfacial and boundary parameters, half-cycle duration

Due to the lack of experimental data regarding interfacial bonds between APs and SE in SSB, and the effect of mechanical interfacial opening on interfacial diffusivity, corresponding parameters required for the simulations are assumed.

First of all, two values of maximum interfacial traction (t_0) are considered – 0.5 and 0.2 MPa – at reference opening $\chi_0 = 0.04\mu$m, see Fig. 2. These values correspond to stiff and soft interfaces, respectively, with initial interfacial stiffness (defined as a gradient of traction-separation law (9) at $\chi = 0$) being 34 and 13.6 MPa/μm. Initial interfacial diffusivity (D_{int}^0) is chosen to be $0.025\,\mu$m/s for 5C rate of charge (C-rate) with $\chi_0^{max} = 0.042\mu$m, see Fig. 3. Typically, in order to charge/discharge a battery at a slower or faster C-rate, the values of the applied current density and cycle duration are proportionally changed. The interfacial flux is driven by the evolution of the electric field which, in turn, depends on the value of the applied current density, see e.g. [10]. Therefore, the interfacial flux is affected by the C-rate. Since the electric field is not considered in the present study, the interfacial flux is assumed to be proportional to the C-rate through the value of initial interfacial diffusivity (D_{int}^0), i.e. 0.004 and 0.0008μm/s are considered for 1C and 5/C rates, respectively. Based on the theoretical time of reaching the full capacity of NMC reported in [10], a chosen value for a half-cycle simulation duration (τ) is 720 s for 5C charging rate, and, hence, 1 h and 5 h for 1C and C/5 rates, respectively, with the same duration assumed both for charge and discharge. A value of $3\,\mu$m/s is set for boundary diffusivity (D_b).

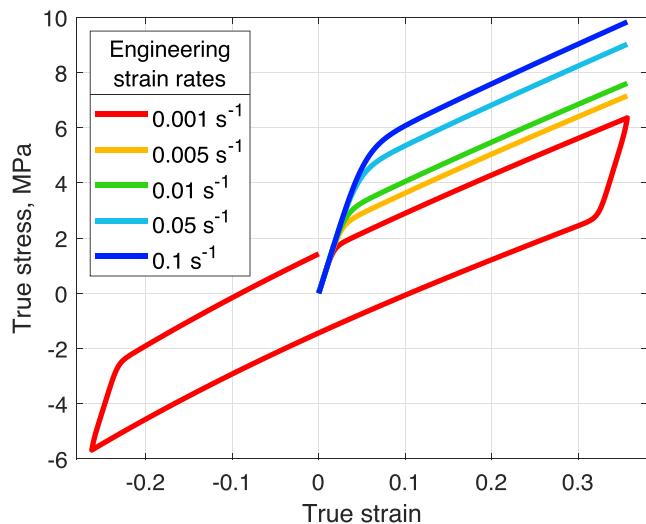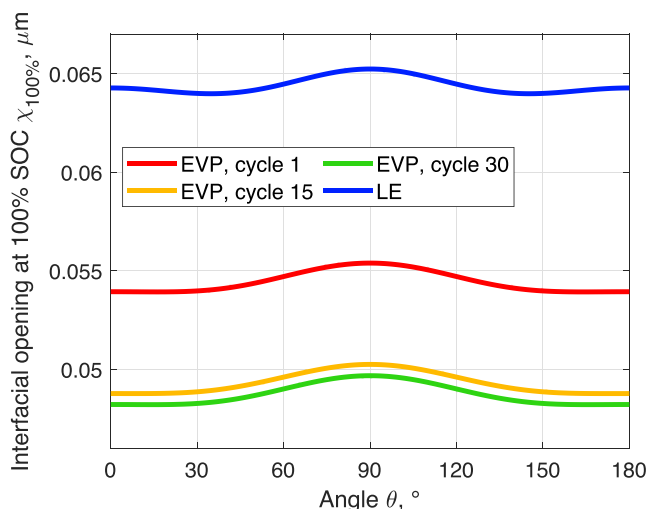**Fig. 5.** Interfacial opening at 100% SOC *vs* angle (see Fig. 1(c) for its definition) for benchmark unit cell size, constant interfacial diffusivity and a stiff interface at 5C charging rate.
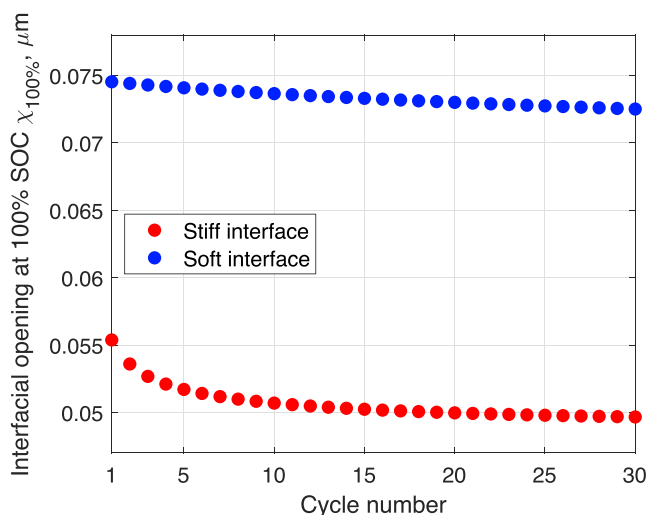

Fig. 6. Interfacial opening at $\theta = 90°$ and 100% SOC *vs* cycle number for the EVP model and benchmark unit cell size with constant interfacial diffusivity at 5C charging rate.

5. Model implementation, results and discussion

5.1. Model implementation

Numerical implementation of the coupled diffusion-mechanics model introduced above, is carried out by means of the nonlinear finite element framework, and integrated with solver ABAQUS. Since mass diffusion analysis available in ABAQUS does not allow for a coupling with mechanics, diffusion is often modelled *via* thermal analysis due to diffusion and heat transfer equations similarities, see e.g. [55,56]. Thus, a fully-coupled thermal-mechanical analysis is used. Moreover, it allows defining specific thermal constitutive behaviour with the help of user subroutine UMATHT, which may be useful in the future for implementation of more rigorous expression for the bulk Li flux instead of Fick's 1st law as discussed in Subsection 3.2.1. The interfacial interactions of the AP and SE are implemented *via* surface-to-surface contact with "master"/"slave" approach (surfaces of AP and surrounding SE correspond to the "master" and "slave" ones, respectively). Additionally, user subroutine UINTER is used for the implementation of the specific interfacial conditions in terms of mechanics, diffusion and

their coupling, see (9), (10), (16) and Subsection 3.3. This approach was adapted in [57] for implementation of cohesive laws. Diffusive boundary condition (17) is employed through standard prescribed boundary convection. The EVP material (constitutive) model proposed for simulation of SE mechanical behaviour, see Subsection 3.1.1, requires the use of user subroutine UMAT. The details on UINTER and UMAT subroutines implementation are provided in Appendix.

5.2. LE vs EVP behaviour of SE

As discussed in Section 1, LE constitutive model is commonly proposed for the description of the SE mechanical response. However, such a simplified approach may be insufficient in the case of a polymer-based SE since even relatively small volumetric changes of APs can cause SE to undergo plasticity. In order to demonstrate this, LE and EVP models are compared in this Subsection. An idealised case of constant interfacial diffusivity (case (1) in Fig. 3) is considered with a stiff interface (interfacial stiffness of 34 MPa/μm corresponding to the maximum traction $t_0 = 0.5$MPa, see Subsection 4.4) at 5C charging rate ($D_{int}^0 = 0.025$μm/s, $\tau = 0.2$ h) and different cycles (shown for the EVP response only since the corresponding curves for the LE model visually coincide) for a benchmark unit cell size (10 μm by 20 μm). An interfacial opening displacement at 100% SOC (maximum AP shrinkage) is denoted as $\chi_{100\%}$ and plotted in Fig. 5 with respect to angle θ (see Fig. 1(c) for θ definition) for LE and EVP models for SE. In general, $\chi_{100\%}$ is smaller for the EVP model with the minimum difference in $\chi_{100\%}$ (between LE and EVP, cycle 1) of $\approx 15\%$ at $\theta \approx 60°$ and 120°, and the maximum one of $\approx 16\%$ at $\theta \approx 0°$ and 180°. This indicate that SE is more compliant in this case, i.e. SE reached its plasticity regime within the given loading range. Moreover, with further cycling, $\chi_{100\%}$ decreased
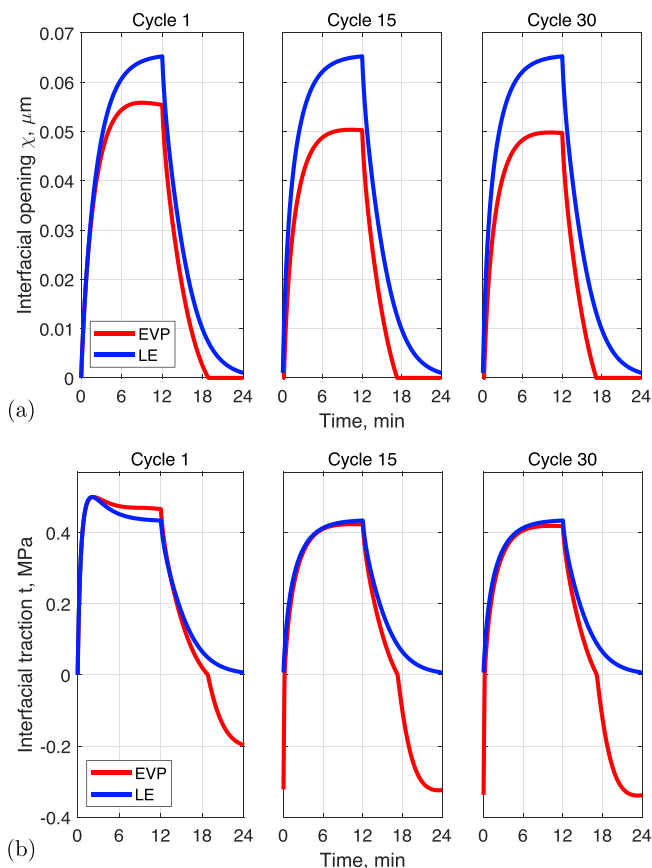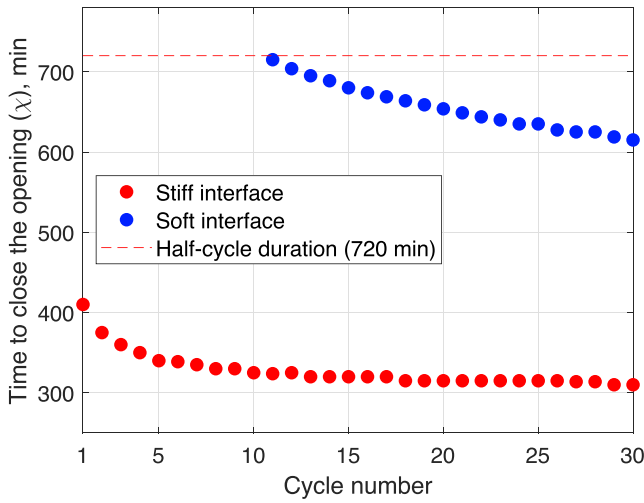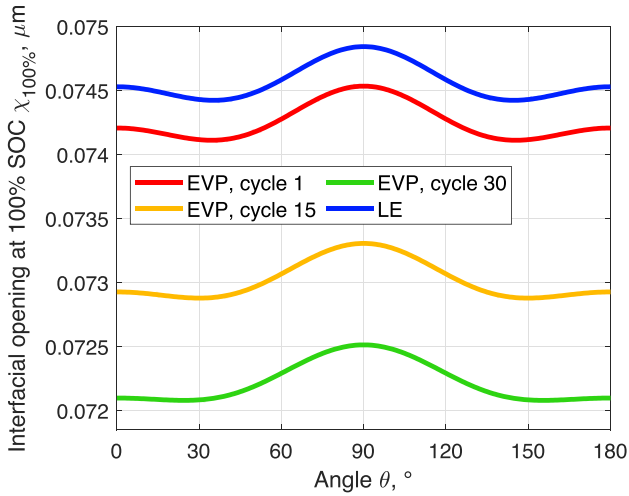

Fig. 7. (a) Interfacial opening displacement and (b) traction variations at $\theta = 90°$ for benchmark unit cell size, constant interfacial diffusivity and a stiff interface at 5C charging rate.

Fig. 8. Time required for closing the interfacial gap at $\theta = 90°$ *vs* cycle number for the EVP model and benchmark unit cell size with constant interfacial diffusivity at 5C charging rate.

Fig. 9. Interfacial opening at 100% SOC *vs* angle (see Fig. 1(c) for its definition) for a soft interface (constant interfacial diffusivity, benchmark unit cell size, 5C charging rate).

for the EVP model due to accumulation in residual plastic strain. This is also shown in Fig. 6 where $\chi_{100\%}$ at $\theta = 90°$ is plotted for the EVP model with respect to the cycle number.

Similar observations can be drawn by analysing the variations of interfacial opening χ and traction t at $\theta = 90°$ over time plotted in Fig. 7 at cycles 1, 15 and 30. For the AP shrinkage (charge half-cycle), χ increases at a similar rate for both SE material models until it enters the plastic regime for the EVP model. Then, the growth rate slows down and χ reaches its peak corresponding to $\chi_{100\%}$ with a smaller value for the EVP model compared to the LE one. Upon AP swelling (discharge half-cycle), the faster decrease of χ in the case of the EVP model is followed by compression (as shown by negative traction) once the interfacial gap has closed. This indicates the presence of the residual plastic strain in the SE as discussed above. Its accumulation with cycling can be seen from the extent of the region where $\chi = 0$ (closed interfacial gap) which becomes wider with cycling. In other words, time required for closing the opening during discharge is getting smaller with cycling, see Fig. 8.

5.3. Effect of interfacial stiffness variation

The effect of the interfacial stiffness on mechanical opening χ is studied here for LE and EVP models at different cycles. For a softer interface with interfacial stiffness of 13.6 MPa/μm (maximum interfacial traction $t_0 = 0.2$MPa), $\chi_{100\%}$ is larger compared to a stiffer interface discussed in the previous Subsection – compare Figs. 5 and 9. This implies that upon AP shrinkage/swelling the softer interface deforms more than the stiffer one and, consequently, the SE deforms less. Therefore, SE plasticity is smaller or has not yet been activated in the case of a softer interface resulting in SE behaviour being closer to the linear elasticity. Thus the difference in χ between LE and EVP models is smaller, which is clearly visible in Fig. 10, where opening χ and traction t are plotted as functions of time (compare with Fig. 7). This difference starts to increase slightly with the number of cycles – again, due to the SE undergoing some plasticity (still smaller than in the case of the stiffer interface), which accumulates with cycling, see Figs. 6 and 8. Note, that the interfacial gap does not close upon swelling of the AP within the half-cycle duration of 720 s for the first 10 cycles, see Fig. 8.
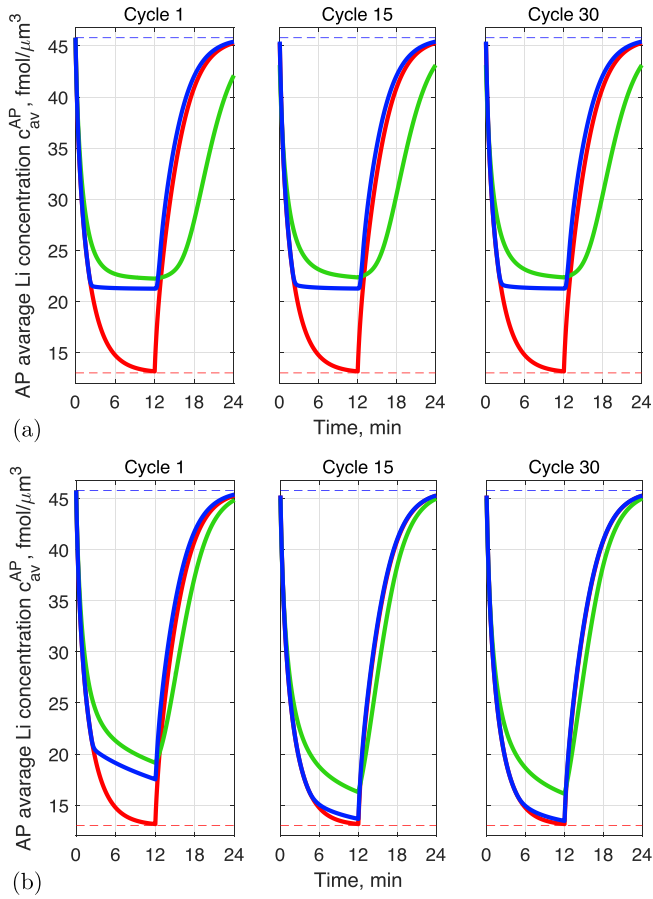
5.4. Effect of interfacial diffusivity variation

In this Subsection, the effect of χ-dependent interfacial diffusivity variation on the average Li concentration in the AP is investigated based on the interfacial transport laws introduced in Subsection 3.3 (see Fig. 3). The AP average Li concentration c_{av}^{AP} is plotted with solid lines
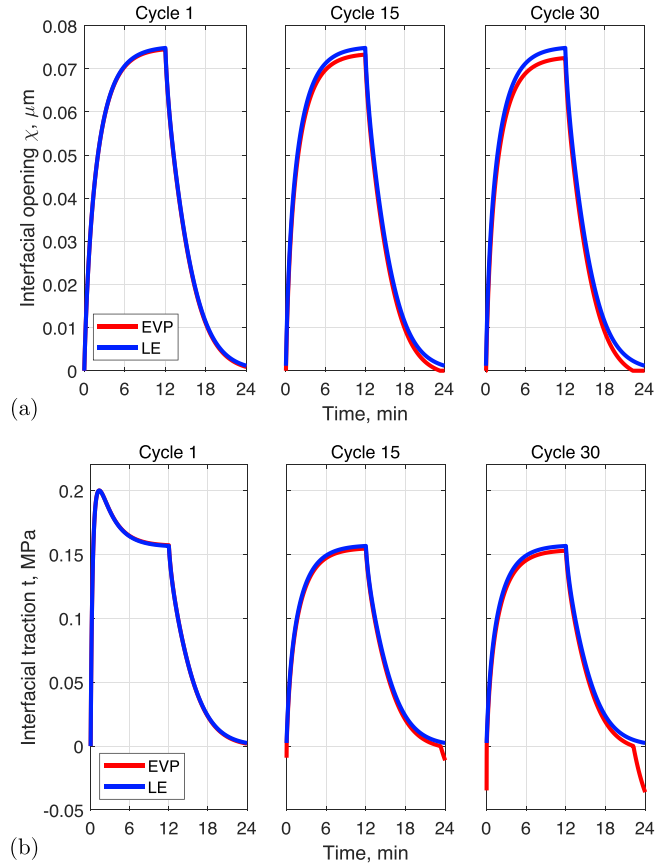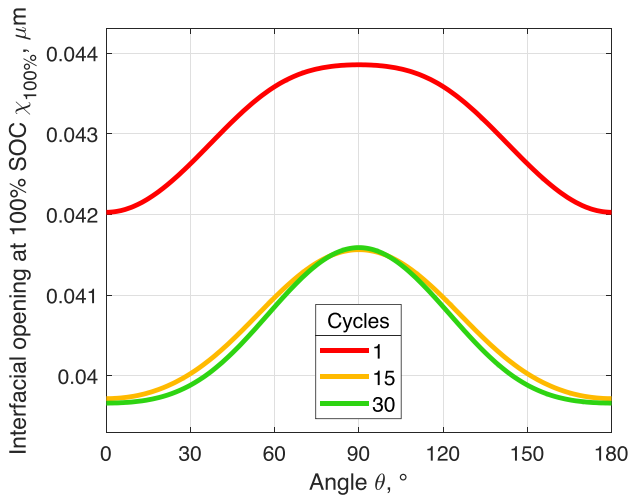

Fig. 10. (a) Interfacial opening displacement and (b) traction variations at $\theta = 90°$ for a soft interface (constant interfacial diffusivity, benchmark unit cell size, 5C charging rate).
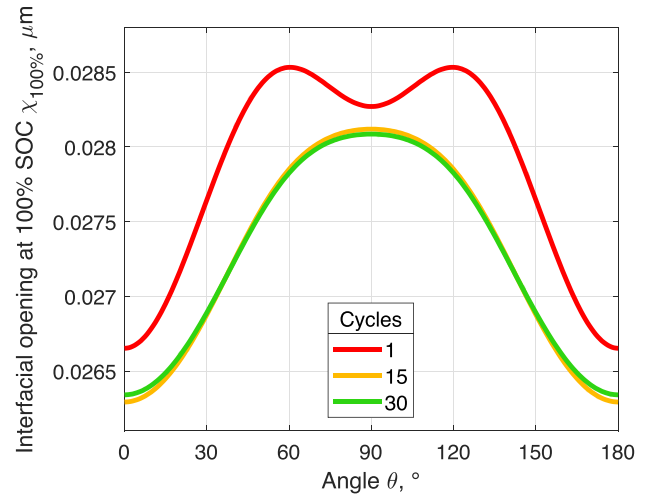
Fig. 11. Charge and discharge curves affected by variation of χ-dependent interfacial diffusivity for (a) LE and (b) EVP models of SE (stiff interface, benchmark unit cell size, 5C charging rate).

Fig. 12. Variation of interfacial opening at 100% SOC at 1C charging rate (EVP model, constant interfacial diffusivity, stiff interface, benchmark unit cell size).

Fig. 13. Variation of interfacial opening at 100% SOC at C/5 charging rate (EVP model, constant interfacial diffusivity, stiff interface, benchmark unit cell size).

– constant with decay, green – case (3) – instant decay. Dashed blue and red lines represent $c_{0\%}^{AP}$ and $c_{100\%}^{AP}$, respectively. Here, the average lithium concentration is determined through volumetric averaging as $c_{av}^{AP} = \frac{1}{N} \sum_{1}^{n} c_{n}^{AP} V_n$ with c_{n}^{AP} and V_n denoting Li concentration and volume at nth integration point (output IVOL in ABAQUS), respectively, and N indicating the number of integration points in the AP instance. As expected, AP average Li concentration is adversely affected by χ through interfacial diffusivity variation. In particular, it results in smaller values of c_{av}^{AP}, i.e. the AP is unable to reach its maximum capacity. Moreover, green curves in Fig. 11(a) for LE model indicate that AP delithiates/lithiates a little slower/faster at cycle 15 compared to cycle 1. This is due to the interface having a reduced stiffness upon unloading and secondary loading caused by the evolution of the interfacial damage, see Fig. 2, leading to a faster gap opening/closure. Also, since χ tends to get smaller with cycling for the EVP model, see Subsections 5.2 and 5.3, it results in an increase of AP average concentration in the cases where the interfacial flux depends on the opening, see the green and blue curves in Fig. 11(b).

5.5. Effect of the C-rate

The C-rate representing a rate at which the battery is charged/discharged has an influence on the half-cycle duration (τ) and interfacial flux ($\vec{j}_{int}$) which is approximated by the variation of the initial interfacial diffusivity value (D_{int}^{0}), see Subsection 4.4 for more detail. The variation of the interfacial flux, in turn, affects the rate of the AP shrinkage/swelling, which has an impact on the mechanical response of the surrounding viscoelastic medium such as polymer-based SE and thus, on the interfacial mechanical response. In other words, slower C-rates correspond to smaller strain rates imposed on SE during shrinkage/swelling of the AP leading to a smaller value of the yield stress, see Fig. 4. Therefore, for slower C-rates, smaller strain is required for the SE to reach its plasticity and become more compliant. This leads to a larger SE deformation and smaller interfacial opening at maximum AP shrinkage $\chi_{100\%}$. As a result, $\chi_{100\%}$ is getting smaller with the decrease of a C-rate, compare Figs. 5, 12 and 13. Moreover, the difference in $\chi_{100\%}$ between cycles 1, 15 and 30 is also getting smaller with the decrease of C-rate, i.e. the effect of subsequent cycling at slower C-rates on SE and, thus, interface states of deformation is less significant. The C-rate can also affect the $\chi_{100\%}$ over θ profile, see e.g. the curve for cycle 1
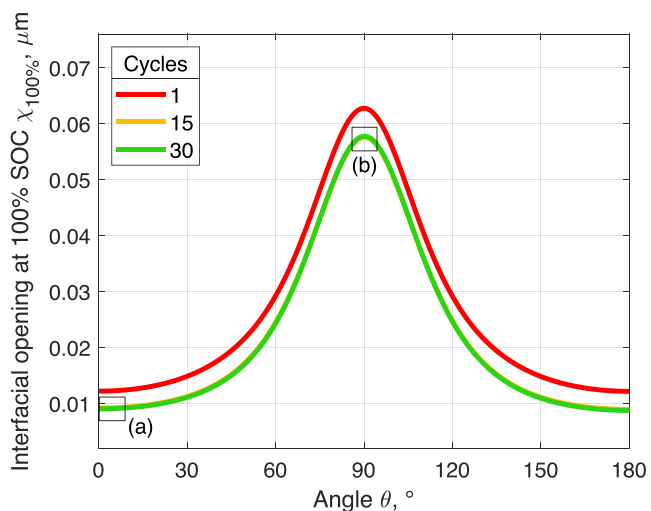
in Fig. 11 as a function of time for the LE and EVP models, where the colours correspond to the ones used in Fig. 3 for different cases of interfacial transport laws, i.e. red – case (1) – constant D_{int}, blue – case (2)

Fig. 14. Interfacial opening at 100% SOC *vs* angle for an ellipsoidal AP (EVP model, constant interfacial diffusivity, stiff interface, benchmark unit cell size, 5C charging rate).
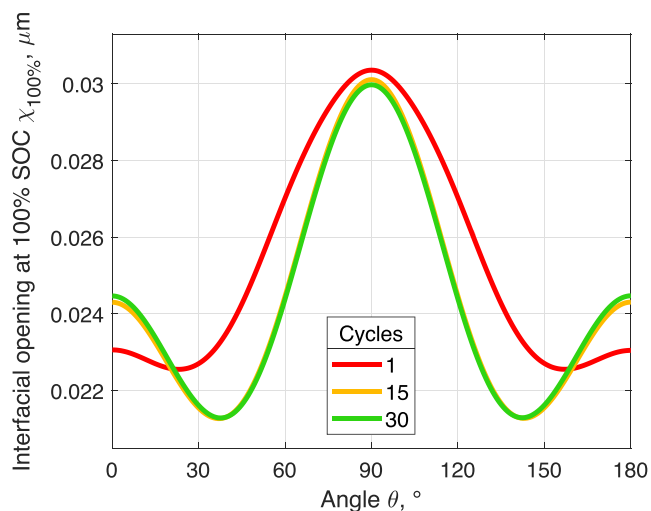

Fig. 16. Interfacial opening at 100% SOC *vs* angle for the unit cell size of $6.5\,\mu m$ and $13\,\mu m$ (EVP model, constant interfacial diffusivity, stiff interface, benchmark unit cell size, 5C charging rate).
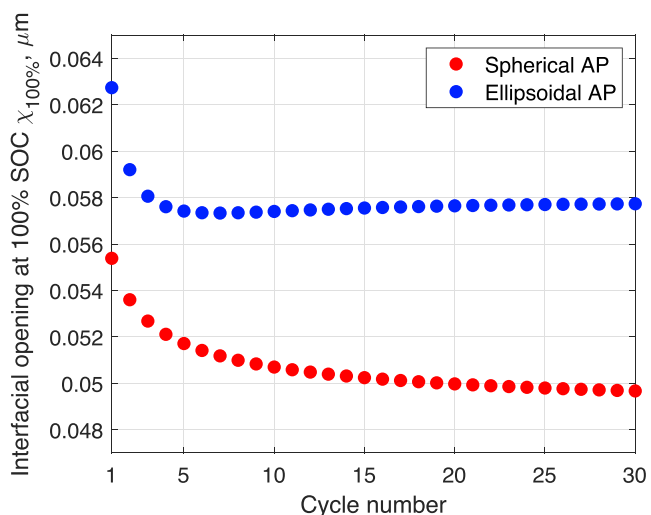

Fig. 15. Interfacial opening at $\theta = 90°$ and 100% SOC *vs* cycle number (EVP model, constant interfacial diffusivity, stiff interface, benchmark unit cell size, 5C charging rate).

Fig. 17. Interfacial opening at 100% SOC *vs* angle for the unit cell size of $5.5\,\mu m$ and $11\,\mu m$ (EVP model, constant interfacial diffusivity, stiff interface, benchmark unit cell size, 5C charging rate).

in Fig. 13. It is also worth mentioning here that the value of the AP Li diffusion coefficient affects the SE response similarly to the C-rate, in particular, its smaller values cause slower diffusion in the AP and thus, an increased time required for the AP to delithiate/lithiate, which is an analogy of slowing down the C-rate. .

5.6. AP aspect ratio variation

SEM images of NMC material reported in e.g. [10,46] show that realistic APs are not perfectly spherical. Therefore, in order to study the effect of a deviation from the spherical shape on the opening χ, an ellipsoidal AP shape is considered in this Subsection with semi-width a and semi-height b, see Fig. 1(c), selected as 6 and $4\,\mu m$, respectively. The simulations show that the AP shape affects the $\chi_{100\%}$ over θ profile, compare Figs. 5 and 14, and the change in this profile with cycling, in particular, for ellipsoidal AP it is not as uniform as in the case of a spherical one, i.e. $\chi_{100\%}$ decreases more substantially at e.g. $\theta = 0°$ and
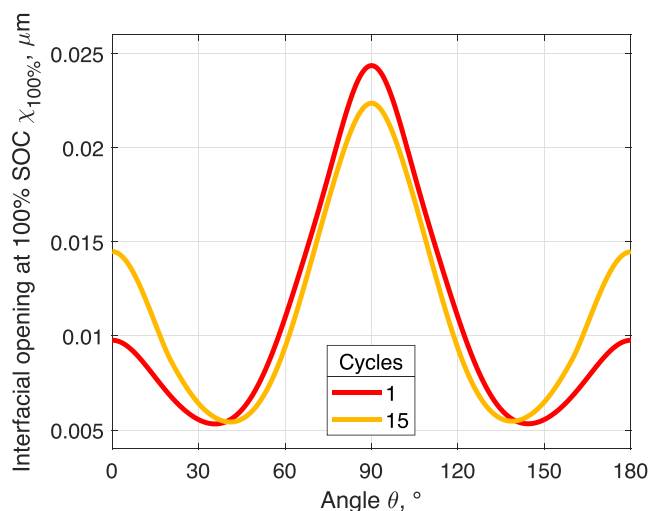
$180°$ compared to $\theta = 75°$. The decrease of $\chi_{100\%}$ with cycling at $\theta = 90°$, however, is similar for spherical and ellipsoidal shapes of the AP, see Fig. 15.

5.7. Effect of active material volume fraction

The impact of active material volume fraction on the interfacial opening is studied by varying the unit cell size. The variations of $\chi_{100\%}$ are plotted with respect to angle θ in Figs. 16 and 17 for smaller unit cell dimensions of $6.5\,\mu m$ by $13\,\mu m$ and $5.5\,\mu m$ by $11\,\mu m$, respectively. Comparison with the results for a benchmark unit cell size ($10\,\mu m$ by $20\,\mu m$) presented in Fig. 5 shows that in general, smaller unit cell dimensions (i.e. higher AP volume fractions) result in smaller values of $\chi_{100\%}$, i.e. SE reaches its plasticity faster, and thus it becomes more compliant earlier, in the case of higher active material volume fraction. The unit cell size also affects the change in the $\chi_{100\%}$ over θ profile with cycling, in particular, $\chi_{100\%}$ decreases at $\theta \approx 90°$ and increases at $\theta \approx 0°$ and $90°$ for smaller unit cell sizes whereas it uniformly decreases for all
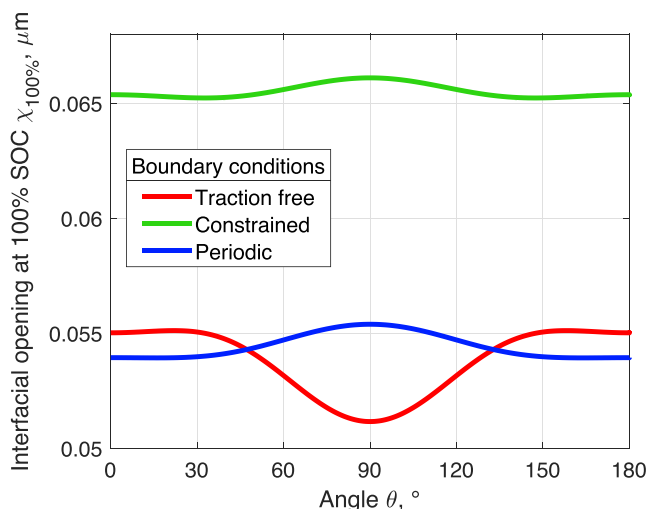
Fig. 18. Interfacial opening at 100% SOC for a unit cell of a benchmark size (EVP model, cycle 1, constant interfacial diffusivity, stiff interface and 5C charging rate).
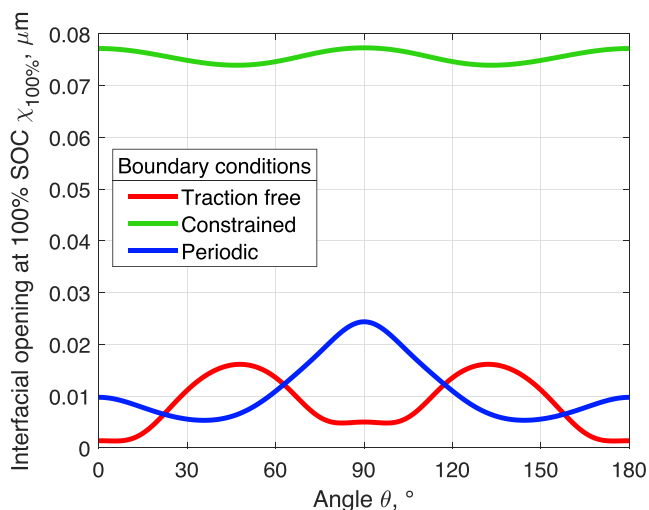

Fig. 19. Interfacial opening at 100% SOC for a unit cell of a smaller size of 5.5 μm and 11 μm (EVP model, cycle 1, constant interfacial diffusivity, stiff interface and 5C charging rate).

θ in the case of a benchmark unit cell size. Note, that cycle 30 is not shown on Fig. 17 since the corresponding curve coincide with the one for cycle 15.

5.8. Effect of unit cell boundary conditions

As discussed in Subsection 3.1.3, *periodic boundary conditions* are applied to the unit cell in order to account for its periodicity within the cathode. In this section unit cells with *traction-free* and *partially-constrained* boundaries are studied. The latter infers that $u_2 = 0$ is set at the upper and lower boundaries of the unit cell (lines AB and CD on Fig. 1c) and and $u_1 = 0$ is applied to the right hand side boundary (line BC). Such conditions allow keeping the unit cell boundaries flat, thus, implying the unit cell periodicity, and are often proposed instead of

periodic ones, see e.g. [58]. The variations of $\chi_{100\%}$ *vs* angle θ for a unit cell of a benchmark size with *traction-free*, *partially-constrained* and *periodic boundary conditions* (EVP model, cycle 1) are plotted in Fig. 18. Constraints applied to the unit cell boundaries result in higher values of the interfacial opening $\chi_{100\%}$ since the SE becomes less compliant. In other words, such boundary conditions overstiffen the SE response, especially if a smaller unit cell size is considered, compare Figs. 18 and 19. The values of the opening $\chi_{100\%}$ in the case of traction-free boundary conditions, in turn, are closer to those for the unit cell with applied periodic boundary conditions. However, since traction-free boundary conditions do not account for the unit cell periodicity, the SE state of deformation is obviously different, as shown by a profile of $\chi_{100\%}$ over θ. It is also worth mentioning that the deformation of more complex statistically representative unit cells (RVEs) with multiple randomly positioned APs may be much less uniform and nonsymmetrical compared to the unit cells with regularly positioned APs making the use of partially-constrained boundary conditions (resulting in flat boundaries) insufficient especially for smaller unit cell sizes. Moreover, in those cells/volumes with multiple APs both partially-constrained and traction-free boundary conditions are unable to account for field fluctuations at the microscale, while the periodic boundary conditions can easily capture them (at least as periodic microfluctuations).

6. Conclusions

Thermoplastic polymers and their composites have been extensively studied as SE materials for SSBs with a particular interest on improving ionic conductivity and mechanical response of polymeric SEs. The present paper contributes to an ongoing discussion on what optimum properties of polymer SE in SSBs should be – in addition to the general knowledge that "softer" systems (i.e. those typically containing lithium salts) exhibit higher ionic conductivity, while "harder" ones prevent from (or delay) dendrite growth, this work shows that yet another aspect should be taken into consideration i.e. ability of SE to accommodate volumetric changes of APs and maintain contact with them throughout the charge-discharge process. The latter can be achieved with SEs that have sufficiently low yield strength generating plastic flow at smaller stresses, which can contribute to the integrity of various interfaces in SSBs.

In the present study, the focus is on providing a fresh insight into the effects of viscoplastic behaviour of a polymer-based SE on the evolution of interfacial damage in a SSB cathode by developing and utilising a non-linear computational microscale diffusion-mechanics model. For this, a BVP is formulated using a simple axisymmetric unit cell concept at the microscale with an elasto-viscoplastic constititive model capturing a non-linear and rate-dependent response of a polymeric SE during SSB cycling, a non-linear cohesive zone concept (traction-separation law), and diffusion-mechanics coupling *via* Vegard's law and interfacial opening-dependent flux. The BVP is integrated into the nonlinear finite-element solver ABAQUS using its user subroutines UMAT and UINTER.

The simulation results show that plastic deformation and residual plastic strains resulting from the SE deformation have a significant effect on the interfacial opening displacement. Particularly, the plastic deformation induced during AP shrinkage may minimise as well as maximise the interfacial opening depending on the problem formulation (AP shape, unit cell size, C-rate, etc), which may be crucial in terms of maintaining interfacial diffusivity. The results demonstrate that slower charging rates lead to a softer SE response and smaller interfacial opening displacement due to the relaxation of the SE caused by its

non-linear viscoelastic nature. Fast C-rates, in turn, can stiffen the mechanical response of the SE, which can lead to higher stresses and a possibility of premature damage. Additional simulations demonstrate that the interfacial stiffness affects plastic deformation of the SE, and hence, the interfacial opening. This indicates the importance of tuning the strength of the interfacial bonding between APs and SE within SSB cathodes to control interfacial damage, and thus Li transport. It is also shown that the values of the interfacial opening are lower for smaller unit cell sizes (i.e. higher AP volume fractions) since the SE reaches its plasticity earlier in cases of higher volume fractions of the active material. Moreover, it is revealed that the partially-constrained boundary conditions, which are frequently used in the battery modelling-related literature, do not capture the actual in situ behaviour at the microscale, and may lead to an overstiffened SE response and, thus, overpredicted values of the interfacial opening, especially for small unit cell sizes.

In general, it is demonstrated that the interfacial opening profile along AP circumference and its change with cycling due to the SE viscoplastic response is sensitive to the AP shape, C-rate, active material volume fraction (unit cell size) and boundary conditions, and therefore, these effects should be further investigated in the context of more realistic and complex microstructures.

Ultimately, a comparison with the linear elastic model for the SE shows that even 5% volumetric shrinkage of the AP results in an overprediction of the interfacial opening displacement value as opposed to a more realistic elasto-viscoplastic behaviour implemented in this paper for the SE. Hence, the use of the linear elastic model may become invalid in the analysis of polymer-based SSBs, when their material components exhibit a non-linear viscoplastic behaviour, especially in the cases of more significant volumetric changes of APs and polymer SEs with smaller values of the yield strength.

Declaration of Competing Interest

The authors declare that they have no known competing financial interests or personal relationships that could have appeared to influence the work reported in this paper.

Appendix A. Notation

Vectors are denoted with an arrow, e.g. $\vec{a}$. Second-order tensors are denoted as bold capital letters $\boldsymbol{A}$ and represent a tensor product between vectors denoted by $\vec{a}\,\vec{b}$. In the index notation it is given by $A_{ij} = a_i b_j$, where A_{ij}, a_i and b_j are components of $\boldsymbol{A}$, $\vec{a}$ and $\vec{b}$, respectively. Fourth-order tensors are formed by a tensor product of four vectors, e.g. $\vec{a}\,\vec{b}\,\vec{c}\,\vec{d}$, or two second-order tensors, e.g. $\boldsymbol{AB}$, and denoted with preceding superscript "4", e.g. $^4\boldsymbol{A}$. The scalar product is denoted with a dot, e.g. $c = \vec{a}\cdot\vec{b}$ for vectors, $\vec{c} = \boldsymbol{A}\cdot\vec{b}$ for a scalar product of a tensor by a vector from the right, and $\boldsymbol{C} = \boldsymbol{A}\cdot\boldsymbol{B}$ in case of two tensors. It can be rewritten in the index notation as $c = a_i b_i$, $c_i = A_{ij} b_j$ and $C_{ij} = A_{ik} B_{kj}$, respectively, with the Einstein summation notation adopted. The double inner product of two tensors is denoted as $c = \boldsymbol{A} : \boldsymbol{B}$ which is $c = A_{ij} B_{ji}$ in the index notation. The transpose of a tensor is denoted as $\boldsymbol{C} = \boldsymbol{A}^T$ and given by $C_{ij} = A_{ji}$ in the index notation. Inverse tensors are denoted with superscript "− 1", e.g. $\boldsymbol{A}^{-1}$, trace and determinant of a tensor are denoted as $\mathrm{tr}(\boldsymbol{A})$ and $\det(\boldsymbol{A})$, respectively.

Standard second- and fourth-order identity tensors and a right transpose of the latter are denoted as $\boldsymbol{I}$, $^4\boldsymbol{I} = \vec{e_i}\,\vec{e_j}\,\vec{e_j}\,\vec{e_i}$, and $^4\boldsymbol{I}^{RT} = \vec{e_i}\,\vec{e_j}\,\vec{e_i}\,\vec{e_j}$, respectively, where $\vec{e_i}$ are basis vectors. Some useful properties are $^4\boldsymbol{I} : \boldsymbol{A} = \boldsymbol{A}$: $^4\boldsymbol{I} = \boldsymbol{A}$ and $^4\boldsymbol{I}^{RT} : \boldsymbol{A} = \boldsymbol{A}$: $^4\boldsymbol{I}^{RT} = \boldsymbol{A}^T$.

The derivatives of function $\varphi = \varphi(\boldsymbol{A})$ and tensor $\boldsymbol{B} = \boldsymbol{B}(\boldsymbol{A})$ with respect to tensor $\boldsymbol{A}$ can be written as

$$\frac{\partial \varphi}{\partial \boldsymbol{A}} = \frac{\partial \varphi}{\partial A_{ij}} \vec{e_i}\,\vec{e_j}, \qquad \frac{\partial \boldsymbol{B}}{\partial \boldsymbol{A}} = \frac{\partial B_{ij}}{\partial A_{km}} \vec{e_i}\,\vec{e_j}\,\vec{e_k}\,\vec{e_m},$$

(A.1)

see [59,60], therefore, the following expressions hold

$$\frac{\partial \boldsymbol{A}}{\partial \boldsymbol{A}} = {}^4\boldsymbol{I}^{RT},$$

$$\frac{\partial \varphi}{\partial \boldsymbol{A}} = \left(\frac{\partial \varphi}{\partial \boldsymbol{Q}}\right)^T : \frac{\partial \boldsymbol{Q}}{\partial \boldsymbol{A}}, \qquad \frac{\partial \boldsymbol{B}}{\partial \boldsymbol{A}} = \frac{\partial \boldsymbol{B}}{\partial \boldsymbol{Q}} : {}^4\boldsymbol{I}^{RT} : \frac{\partial \boldsymbol{Q}}{\partial \boldsymbol{A}},$$

$$\frac{\partial (\mathrm{tr}(\boldsymbol{A}))}{\partial \boldsymbol{A}} = \boldsymbol{I}, \qquad \frac{\partial (\det(\boldsymbol{A}))}{\partial \boldsymbol{A}} = \det(\boldsymbol{A})\boldsymbol{A}^{-T},$$

$$\frac{\partial (\boldsymbol{A}^{-1})}{\partial \boldsymbol{A}} = -\boldsymbol{A}^{-1} \cdot {}^4\boldsymbol{I}^{RT} \cdot \boldsymbol{A}^{-T}.$$

(A.2)

In addition, it is useful to note that

$$\frac{\partial (\varphi \boldsymbol{B})}{\partial \boldsymbol{A}} = \varphi \frac{\partial \boldsymbol{B}}{\partial \boldsymbol{A}} + \boldsymbol{B}\frac{\partial \varphi}{\partial \boldsymbol{A}}, \qquad \frac{\partial (\boldsymbol{A}\cdot\boldsymbol{Q}\cdot\boldsymbol{B})}{\partial \boldsymbol{Q}} = \boldsymbol{A} \cdot {}^4\boldsymbol{I}^{RT} \cdot \boldsymbol{B}^T,$$

$$\boldsymbol{I} : (\boldsymbol{A}\cdot {}^4\boldsymbol{I}^{RT}\cdot\boldsymbol{B}) = \boldsymbol{A}^T \cdot \boldsymbol{B}.$$

(A.3)

Appendix B. List of abbreviations

LIB	Li-ion battery
AP	Active particle
SSB	Solid state battery
SE	Solid electrolyte
LE	Linear elastic
EVP	Elasto-viscoplastic
BVP	Boundary value problem
PEO	Poly(ethylene oxide)
NMC	Lithium Nickel Manganese Cobalt Oxide

Appendix C. UINTER subroutine implementation

As discussed in Subsection 5.1, traction-separation law (9) with the expression governing its unloading (10), interfacial diffusivity condition (16) and the coupling between interfacial flux and normal opening displacement introduced in Subsection 3.3, are implemented in UINTER subroutine.

The subroutine passes in interfacial stress components STRESS(i) at the beginning of an increment in the local coordinate system, which then need to be updated depending on the given relative positions between surfaces RDISP(i) with $i = 1, 2$ denoting normal and shear directions, respectively. Negative values of RDISP(1) and STRESS(1) correspond to opening and tension. The loading and unloading regimes in the traction-separation law are determined by the value of DRDISP(1) – an increment in relative position between surfaces – with RDISP(1) < 0 and DRDISP (1) < 0 indicating tensile loading and unloading, respectively. At the same time, penetration of the AP into the SE defined by positive value of RDISP(1) is prevented using penalty compressive stress

$$t = k_p \chi \tag{C.1}$$

represented by positive STRESS(1) with k_p being a penalty coefficient. As a result, a check for the values of RDISP(1) and DRDISP(1) is undertaken with every call of UINTER, leading to the use of the corresponding law (either (9), (10) or (C.1)) for the interfacial stresses components STRESS(i) update.

Interfacial condition (16) is implemented through the update of heat flux (analogy of interfacial Li flux $\overrightarrow{j_{int}}$) magnitudes FLUX(j) into the "slave" ($j = 1$) and "master" ($j = 2$) surfaces, depending on both mechanical openings RDISP(i) (through interfacial diffusivity D_{int}, see Subsection 3.3) and surface temperatures (analogy of concentrations c_{int}^{SE} and c_{int}^{AP}) TEMP(j). Here, positive and negative values of the flux indicate heat flowing into and out of the surface, respectively.

Finally, DDSDDR(i, i), DDSDDT(i, j), DDFDDT(j, j) and DDFDDR(j, i), which represent variations (or their negatives in case of DDFDDT(j, j)) of stresses STRESS(i) and fluxes FLUX(j) with respect to the relative opening displacements RDISP(i) and temperatures TEMP(j), also need to be provided, see [61] for more detail.

Appendix D. UMAT subroutine implementation

UMAT subroutine is used to implement the non-linear constitutive (material) law for the SE in the framework of finite deformations (see Subsection 3.1.1). Main implementation details are explained below.

D.1. Stress update

First of all, the subroutine requires to update Cauchy stress components STRESS(n), $n = 4$(for an axisymmetric problem in Voigt notation), at the end of each increment. Since finite deformations are considered (option NLGEOM is ON), the total deformation gradient F is passed in at the beginning (τ_n) and at the end ($\tau_{n+1} = \tau_n + \Delta\tau$) of each increment, corresponding to the time duration of $\Delta\tau$. Also, since plastic deformations are not present at the beginning of the analysis, $F_p = I$ and $D_p = 0$ are set to initialise the incremental-iterative solution procedure.

Plastic part of the velocity gradient tensor is given by $L_p = F_e \cdot \dot{F}_p \cdot F_p^{-1} \cdot F_e^{-1}$, therefore, taking into account the multiplicative decomposition of the total deformation gradient ($F = F_e \cdot F_p$), and the fact that the plastic deformation is spin-free $W_p = 0$ ($L_p = D_p$), the plastic part of the deformation rate tensor can be rewritten as

$$D_p = F \cdot F_p^{-1} \cdot \dot{F}_p \cdot F^{-1}. \tag{C.1}$$

Hence, (C.1) can be rearranged as

$$\dot{F}_p^T = \hat{D}_p^T \cdot F_p^T, \tag{C.2}$$

where $\hat{D}_p = F^{-1} \cdot D_p \cdot F$. The scheme for derivation of the solution for F_p^T within an incremental time stepping procedure presented below follows from [62]. It is assumed that $\hat{D}_p$ is constant during an increment, hence, the plastic deformation gradient at the end of the increment is given by

$$F_p^T(\tau_{n+1}) = \tilde{F}_p^T \cdot F_p^T(\tau_n), \tag{C.3}$$

where

$$\widetilde{\boldsymbol{F}}_p^T = \exp[\Delta\tau\widehat{\boldsymbol{D}}_p^T(\tau_n)]. \tag{C.4}$$

Note, that the explicit integration scheme is used, which is only conditionally stable. Various approximations are available for the evaluation of tensor exponential $\widetilde{\boldsymbol{F}}_p^T$, e.g. Padé approximation

$$\widetilde{\boldsymbol{F}}_p^T \approx \left(\boldsymbol{I} - \frac{\Delta\tau}{2}\widehat{\boldsymbol{D}}_p^T\right)^{-1} \cdot \left(\boldsymbol{I} + \frac{\Delta\tau}{2}\widehat{\boldsymbol{D}}_p^T\right) = \widehat{\boldsymbol{F}}_p^T. \tag{C.5}$$

For finite increments, the determinant of the approximated exponential term $\widehat{\boldsymbol{F}}_p^T$ may deviate slightly from unity, which may be corrected by $[\det(\widehat{\boldsymbol{F}}_p^T)]^{-\frac{1}{3}}$. Therefore,

$$\widetilde{\boldsymbol{F}}_p^T = [\det(\widehat{\boldsymbol{F}}_p^T)]^{-\frac{1}{3}}\widehat{\boldsymbol{F}}_p^T. \tag{C.6}$$

As a result, plastic part of the deformation gradient $\boldsymbol{F}_p$ is derived at the end of an increment (τ_{n+1}) and, thus, the elastic part is obtained using $\boldsymbol{F}_e = \boldsymbol{F} \cdot \boldsymbol{F}_p^{-1}$, which allows updating Cauchy stress $\boldsymbol{\sigma}$ and plastic rate of deformation tensor $\boldsymbol{D}_p$ using (2) and (7). Finally, components of $\boldsymbol{\sigma}$ are rewritten in Voigt notation as STRESS(n), see [61] for a particular order of stress components; $\boldsymbol{F}_p$ and $\boldsymbol{D}_p$ are stored as STATEV variables, and passed onto the next increment.

D.1.1. Jacobian (DDSDDE)

Another requirement of UMAT subroutine is to provide Jacobian for the current increment defined by DDSDDE(n, n) in Voigt notation. It is shown in [63] that the consistent fourth-order Jacobian tensor $^4\boldsymbol{J}$ can be derived based on Jaumann rate of Kirchhoff stress. Hence, the components of $^4\boldsymbol{J}$ are defined as

$$
\begin{aligned}
J_{iqph} = {} & \tfrac{1}{J}F_{iM}F_{qI}F_{pK}F_{hL}\frac{\partial S_{MI}}{\partial E_{KL}} \\
& + \tfrac{1}{2}(\sigma_{ip}\delta_{qh} + \sigma_{qh}\delta_{ip} + \sigma_{ih}\delta_{qp} + \sigma_{qp}\delta_{ih}).
\end{aligned} \tag{C.7}
$$

where $i, q, p, h, M, I, K, L = 1, 2, 3$ with lower-case and upper-case indices referring to the current and reference configurations, respectively; S_{MI} and E_{KL} are the components of second Piola-Kirchhoff stress and Green-Lagrange strain tensors, $\boldsymbol{S} = \boldsymbol{F}^{-1} \cdot J\boldsymbol{\sigma} \cdot \boldsymbol{F}^{-T}$ and $\boldsymbol{E} = \frac{1}{2}(\boldsymbol{C} - \boldsymbol{I})$, respectively, where $\boldsymbol{C} = \boldsymbol{F}^T \cdot \boldsymbol{F}$ is the right Cauchy-Green deformation tensor.

Following (2), second Piola-Kirchhoff stress tensor can be written as

$$\boldsymbol{S} = \boldsymbol{S}_v + \boldsymbol{S}_s^d + \boldsymbol{S}_h^d, \tag{C.8}$$

where

$$
\begin{aligned}
\boldsymbol{S}_v &= K(J_e - 1)\boldsymbol{C}^{-1}, \\
\boldsymbol{S}_s^d &= G_s\left(J_e^{-\frac{2}{3}}\boldsymbol{C}_p^{-1} - \tfrac{1}{3}\mathrm{tr}(\bar{\boldsymbol{C}}_e)\boldsymbol{C}^{-1}\right), \\
\boldsymbol{S}_h^d &= G_h\left(J_e^{-\frac{2}{3}}\boldsymbol{I} - \tfrac{1}{3}\mathrm{tr}(\bar{\boldsymbol{C}})\boldsymbol{C}^{-1}\right),
\end{aligned} \tag{C.9}
$$

with

$$
\begin{aligned}
\boldsymbol{C}_p &= \boldsymbol{F}_p^T \cdot \boldsymbol{F}_p, \quad \bar{\boldsymbol{C}}_e = (J_e)^{-\frac{2}{3}}\boldsymbol{F}_e^T \cdot \boldsymbol{F}_e, \quad \bar{\boldsymbol{C}} = (J_e)^{-\frac{2}{3}}\boldsymbol{F}^T \cdot \boldsymbol{F}, \\
\mathrm{tr}(\bar{\boldsymbol{C}}_e) &= \mathrm{tr}(\bar{\boldsymbol{B}}_e), \quad \mathrm{tr}(\bar{\boldsymbol{C}}) = \mathrm{tr}(\bar{\boldsymbol{B}}).
\end{aligned} \tag{C.10}
$$

Therefore,

$$\frac{\partial\boldsymbol{S}}{\partial\boldsymbol{E}} = 2\left(\frac{\partial\boldsymbol{S}_v}{\partial\boldsymbol{C}} + \frac{\partial\boldsymbol{S}_s^d}{\partial\boldsymbol{C}} + \frac{\partial\boldsymbol{S}_h^d}{\partial\boldsymbol{C}}\right), \tag{C.11}$$

where

$$
\begin{aligned}
\frac{\partial\boldsymbol{S}_v}{\partial\boldsymbol{C}} &= K\left((J_e - 1)\,^4\boldsymbol{X} + \frac{J_e}{2}\boldsymbol{C}^{-1}\boldsymbol{C}^{-1}\right), \\
\frac{\partial\boldsymbol{S}_s^d}{\partial\boldsymbol{C}} &= G_s\left[\boldsymbol{C}_p^{-1}\boldsymbol{Y} - \tfrac{1}{3}\left[\mathrm{tr}(\bar{\boldsymbol{C}}_e)\,^4\boldsymbol{X} + \boldsymbol{C}^{-1}\left(J_e^{-\frac{2}{3}}\boldsymbol{C}_p^{-1} + \mathrm{tr}(\boldsymbol{C}_e)\boldsymbol{Y}\right)\right]\right], \\
\frac{\partial\boldsymbol{S}_h^d}{\partial\boldsymbol{C}} &= G_h\left[\boldsymbol{I}\boldsymbol{Y} - \tfrac{1}{3}\left[\mathrm{tr}(\bar{\boldsymbol{C}})\,^4\boldsymbol{X} + \boldsymbol{C}^{-1}\left(J_e^{-\frac{2}{3}}\boldsymbol{I} + \mathrm{tr}(\boldsymbol{C})\boldsymbol{Y}\right)\right]\right],
\end{aligned} \tag{C.12}
$$

with

$$^4\boldsymbol{X} = \frac{\partial\boldsymbol{C}^{-1}}{\partial\boldsymbol{C}} = -\boldsymbol{C}^{-1} \cdot {}^4\boldsymbol{I}^{RT} \cdot \boldsymbol{C}^{-1}, \qquad \boldsymbol{Y} = \frac{\partial J_e^{-\frac{2}{3}}}{\partial\boldsymbol{C}} = -\frac{1}{3}J_e^{-\frac{2}{3}}\boldsymbol{C}^{-1}. \tag{C.13}$$

Here, $^4\mathbf{I}^{RT}$ represent the right transpose of the fourth-order identity tensor (see Appendix A), and

$$J_e = \sqrt{\det(\mathbf{C})}, \qquad \mathbf{C}^{-T} = \mathbf{C}^{-1}, \qquad \mathbf{C}_e = \mathbf{F}_e^T \cdot \mathbf{F}_e. \tag{C.14}$$

At the end, $^4\mathbf{J}$ is obtained using the components of the fourth-order tensor $\frac{\partial S}{\partial E}$ defined in (C.11), deformation gradient and Cauchy stress tensors, $\mathbf{F}$ and σ, respectively. Then, the components of $^4\mathbf{J}$ are rewritten from tensor to Voigt notation as DDSDDE(n, n).

References

[1] J.B. Goodenough, Energy storage materials: a perspective, Energy Storage Mater. 1 (2015) 158–161.

[2] A. Mukhopadhyay, B.W. Sheldon, Deformation and stress in electrode materials for Li-ion batteries, Prog. Mater. Sci. 63 (2014) 58–116.

[3] S. Zhang, Chemomechanical modeling of lithiation-induced failure in high-volume-change electrode materials for lithium ion batteries, NPJ Comput. Mater. 3 (1) (2017) 1–11.

[4] Y. Zhao, P. Stein, Y. Bai, M. Al-Siraj, Y. Yang, B.-X. Xu, A review on modeling of electro-chemo-mechanics in lithium-ion batteries, J. Power Sources 413 (2019) 259–283.

[5] Y.-T. Cheng, M.W. Verbrugge, Diffusion-induced stress, interfacial charge transfer, and criteria for avoiding crack initiation of electrode particles, J. Electrochem. Soc. 157 (4) (2010) A508–A516.

[6] R. Grantab, V.B. Shenoy, Location-and orientation-dependent progressive crack propagation in cylindrical graphite electrode particles, J. Electrochem. Soc. 158 (8) (2011) A948–A954.

[7] A.F. Bower, P.R. Guduru, A simple finite element model of diffusion, finite deformation, plasticity and fracture in lithium ion insertion electrode materials, Modell. Simul. Mater. Sci. Eng. 20 (4) (2012) 045004.

[8] M. Klinsmann, D. Rosato, M. Kamlah, R.M. McMeeking, Modeling crack growth during Li insertion in storage particles using a fracture phase field approach, J. Mech. Phys. Solids 92 (2016) 313–344.

[9] A. Singh, S. Pal, Coupled chemo-mechanical modeling of fracture in polycrystalline cathode for lithium-ion battery, Int. J. Plast. 127 (2020) 102636.

[10] R. Xu, Y. Yang, F. Yin, P. Liu, P. Cloetens, Y. Liu, F. Lin, K. Zhao, Heterogeneous damage in Li-ion batteries: experimental analysis and theoretical modeling, J. Mech. Phys. Solids 129 (2019) 160–183.

[11] R. Koerver, I. Aygün, T. Leichtweiß, C. Dietrich, W. Zhang, J.O. Binder, P. Hartmann, W.G. Zeier, J. Janek, Capacity fade in solid-state batteries: interphase formation and chemomechanical processes in nickel-rich layered oxide cathodes and lithium thiophosphate solid electrolytes, Chem. Mater. 29 (13) (2017) 5574–5582.

[12] R. Koerver, W. Zhang, L. de Biasi, S. Schweidler, A.O. Kondrakov, S. Kolling, T. Brezesinski, P. Hartmann, W.G. Zeier, J. Janek, Chemo-mechanical expansion of lithium electrode materials–on the route to mechanically optimized all-solid-state batteries, Energy Environ. Sci. 11 (8) (2018) 2142–2158.

[13] R.C. Agrawal, G.P. Pandey, Solid polymer electrolytes: materials designing and all-solid-state battery applications: an overview, J. Phys. D: Appl. Phys. 41 (22) (2008) 223001.

[14] G. El-Enany, M.J. Lacey, P.A. Johns, J.R. Owen, In situ growth of polymer electrolytes on lithium ion electrode surfaces, Electrochem. Commun. 11 (12) (2009) 2320–2323.

[15] S. Tan, S. Walus, J. Hilborn, T. Gustafsson, D. Brandell, Poly (ether amine) and cross-linked poly (propylene oxide) diacrylate thin-film polymer electrolyte for 3D-microbatteries, Electrochem. Commun. 12 (11) (2010) 1498–1500.

[16] H. Gupta, S.K. Singh, V.K. Singh, A.K. Tripathi, N. Srivastava, R.K. Tiwari, R. Mishra, D. Meghnani, R.K. Singh, Development of polymer electrolyte and cathode material for Li-batteries, J. Electrochem. Soc. 166 (3) (2019) A5187–A5192.

[17] V. Zadin, D. Brandell, Modelling polymer electrolytes for 3D-microbatteries using finite element analysis, Electrochim. Acta 57 (2011) 237–243.

[18] D. Grazioli, O. Verners, V. Zadin, D. Brandell, A. Simone, Electrochemical-mechanical modeling of solid polymer electrolytes: Impact of mechanical stresses on Li-ion battery performance, Electrochim. Acta 296 (2019) 1122–1141.

[19] D. Grazioli, V. Zadin, D. Brandell, A. Simone, Electrochemical-mechanical modeling of solid polymer electrolytes: Stress development and non-uniform electric current density in trench geometry microbatteries, Electrochim. Acta 296 (2019) 1142–1162.

[20] G. Bucci, T. Swamy, Y.-M. Chiang, W.C. Carter, Modeling of internal mechanical failure of all-solid-state batteries during electrochemical cycling, and implications for battery design, J. Mater. Chem. A 5 (36) (2017) 19422–19430.

[21] G. Bucci, B. Talamini, A.R. Balakrishna, Y.-M. Chiang, W.C. Carter, Mechanical instability of electrode-electrolyte interfaces in solid-state batteries, Phys. Rev. Mater. 2 (10) (2018) 105407.

[22] K. Matouš, M.G.D. Geers, V.G. Kouznetsova, A. Gillman, A review of predictive nonlinear theories for multiscale modeling of heterogeneous materials, J. Comput. Phys. 330 (2017) 192–220.

[23] M. Geers, V. Kouznetsova, W. Brekelmans, Computational homogenization, Multiscale Modelling of Plasticity and Fracture by Means of Dislocation Mechanics, Springer, Vienna, 2010, pp. 327–394.

[24] I. Özdemir, W.A.M. Brekelmans, M.G.D. Geers, Computational homogenization for heat conduction in heterogeneous solids, Int. J. Numer. Meth. Eng. 73 (2) (2008) 185–204.

[25] I. Özdemir, W.A.M. Brekelmans, M.G.D. Geers, FE2 computational homogenization for the thermo-mechanical analysis of heterogeneous solids, Comput. Methods Appl. Mech. Eng. 198 (3–4) (2008) 602–613.

[26] A. Salvadori, E. Bosco, D. Grazioli, A computational homogenization approach for Li-ion battery cells: Part 1–formulation, J. Mech. Phys. Solids 65 (2014) 114–137.

[27] A. Salvadori, D. Grazioli, M.G.D. Geers, D. Danilov, P.H.L. Notten, A multiscale-compatible approach in modeling ionic transport in the electrolyte of (Lithium ion) batteries, J. Power Sources 293 (2015) 892–911.

[28] V. Tvergaard, On localization in ductile materials containing spherical voids, Int. J. Fract. 18 (4) (1982) 237–252.

[29] A.R. Balakrishna, Y.-M. Chiang, W.C. Carter, Phase-field model for diffusion-induced grain boundary migration: An application to battery electrodes, Phys. Rev. Mater. 3 (6) (2019) 065404.

[30] T.A. Tervoort, R.J.M. Smit, W.A.M. Brekelmans, L.E. Govaert, A constitutive equation for the elasto-viscoplastic deformation of glassy polymers, Mech. Time-Dependent Mater. 1 (3) (1997) 269–291.

[31] J.A.W. van Dommelen, D.M. Parks, M.C. Boyce, W.A.M. Brekelmans, F.P.T. Baaijens, Micromechanical modeling of the elasto-viscoplastic behavior of semi-crystalline polymers, J. Mech. Phys. Solids 51 (3) (2003) 519–541.

[32] E.T.J. Klompen, T.A.P. Engels, L.E. Govaert, H.E.H. Meijer, Modeling of the post-yield response of glassy polymers: influence of thermomechanical history, Macromolecules 38 (16) (2005) 6997–7008.

[33] E.H. Lee, D.T. Liu, Finite-strain elastic-plastic theory with application to plane-wave analysis, J. Appl. Phys. 38 (1) (1967) 19–27.

[34] J.H. Rose, J. Ferrante, J.R. Smith, Universal binding energy curves for metals and bimetallic interfaces, Phys. Rev. Lett. 47 (9) (1981) 675.

[35] G.T. Camacho, M. Ortiz, Computational modelling of impact damage in brittle materials, Int. J. Solids Struct. 33 (20–22) (1996) 2899–2938.

[36] A. Salvadori, D. Grazioli, M.G.D. Geers, Governing equations for a two-scale analysis of Li-battery cells, Int. J. Solids Struct. 59 (2015) 90–109.

[37] V. Zadin, H. Kasemägi, A. Aabloo, D. Brandell, Modelling electrode material utilization in the trench model 3d-microbattery by finite element analysis, J. Power Sources 195 (18) (2010) 6218–6224.

[38] P.P. Natsiavas, K. Weinberg, D. Rosato, M. Ortiz, Effect of prestress on the stability of electrode-electrolyte interfaces during charging in lithium batteries, J. Mech. Phys. Solids 95 (2016) 92–111.

[39] G. Bucci, Y.-M. Chiang, W.C. Carter, Formulation of the coupled electro-chemical–mechanical boundary-value problem, with applications to transport of multiple charged species, Acta Mater. 104 (2016) 33–51.

[40] C.-H. Chen, F.B. Planella, K. O'Regan, D.E. Gastol, W.D. Widanage, E. Kendrick, Development of experimental techniques for parameterization of multi-scale lithium-ion battery models, J. Electrochem. Soc. 167 (2020) 080534.

[41] J. Newman, K.E. Thomas-Alyea, Electrochemical Systems, John Wiley & Sons, 2012.

[42] T. Kelly, B.M. Ghadi, S. Berg, H. Ardebili, In situ study of strain-dependent ion conductivity of stretchable polyethylene oxide electrolyte, Scientific Rep. 6 (2016) 20128.

[43] O. Capron, R. Gopalakrishnan, J. Jaguemont, P. Van Den Bossche, N. Omar, J. Van Mierlo, On the ageing of high energy lithium-ion batteries – comprehensive electrochemical diffusivity studies of harvested nickel manganese cobalt electrodes, Materials 11 (2) (2018) 176.

[44] L.S. de Vasconcelos, R. Xu, J. Li, K. Zhao, Grid indentation analysis of mechanical properties of composite electrodes in Li-ion batteries, Extreme Mech. Lett. 9 (2016) 495–502.

[45] R. Weber, C.R. Fell, S. Hy, Operando X-ray diffraction study of polycrystalline and single-crystal $Li_xNi_{0.5}Mn_{0.3}Co_{0.2}O_2$, J. Electrochem. Soc. 164 (13) (2017) A2992–A2999.

[46] R. Xu, H. Sun, L.S. de Vasconcelos, K. Zhao, Mechanical and structural degradation of $LiNi_xMn_yCo_zO_2$ cathode in Li-ion batteries: an experimental study, J. Electrochem. Soc. 164 (13) (2017) A3333–A3341.

[47] A.O. Kondrakov, H. Geßwein, K. Galdina, L. De Biasi, E.O. Filatova, G. Schumacher, W. Wenzel, P. Hartmann, T. Brezesinski, et al., Charge-transfer-induced lattice collapse in Ni-rich NCM cathode materials during delithiation, J. Phys. Chem. C 121 (44) (2017) 24381–24388.

[48] K. Märker, P.J. Reeves, C. Xu, K.J. Griffith, C.P. Grey, Evolution of structure and lithium dynamics in LiNi$_{0.8}$Mn$_{0.1}$Co$_{0.1}$O$_2$ (NMC811) cathodes during electrochemical cycling, Chem. Mater. 31 (7) (2019) 2545–2554.

[49] E.J. Cheng, K. Hong, N.J. Taylor, H. Choe, J. Wolfenstine, J. Sakamoto, Mechanical and physical properties of LiNi$_{0.33}$Mn$_{0.33}$Co$_{0.33}$O$_2$ (NMC), J. Eur. Ceram. Soc. 37(9) (2017) 3213–3217.

[50] D. Lindqvist, Simulation of intermittent current interruption measurements on NMC-based lithium-ion batteries (2017).

[51] R. Amin, Y.-M. Chiang, Characterization of electronic and ionic transport in Li$_{1-x}$Ni$_{0.33}$Mn$_{0.33}$Co$_{0.33}$O$_2$ (NMC$_{333}$) and Li$_{1-x}$Ni$_{0.50}$Mn$_{0.20}$Co$_{0.30}$O$_2$ (NMC$_{523}$) as a function of Li content, J. Electrochem. Soc. 163 (8) (2016) A1512–A1517.

[52] D. Devaux, R. Bouchet, D. Glé, R. Denoyel, Mechanism of ion transport in PEO/LiTFSI complexes: effect of temperature, molecular weight and end groups, Solid State Ionics 227 (2012) 119–127.

[53] M. Mareno, R. Quijada, M.A. Santa Ana, E. Benavente, P. Gomez-Romero, G. González, Electrical and mechanical properties of poly (ethylene oxide)/intercalated clay polymer electrolyte, Electrochim. Acta 58 (2011) 112–118.

[54] J. Karo, D. Brandell, A molecular dynamics study of the influence of side-chain length and spacing on lithium mobility in non-crystalline LiPF$_6$·PEO$_x$; $x = 10$ and 30, Solid State Ionics 180 (23–25) (2009) 1272–1284.

[55] C.-S. Oh, Y.-J. Kim, K.-B. Yoon, Coupled analysis of hydrogen transport using ABAQUS, J. Solid Mech. Mater. Eng. 4 (7) (2010) 908–917.

[56] O. Barrera, E. Tarleton, H.W. Tang, A.C.F. Cocks, Modelling the coupling between hydrogen diffusion and the mechanical behaviour of metals, Comput. Mater. Sci. 122 (2016) 219–228.

[57] S. Feih, Modelling cohesive laws in finite element simulations via an adapted contact procedure in ABAQUS.

[58] W. Wu, X. Xiao, M. Wang, X. Huang, A microstructural resolved model for the stress analysis of lithium-ion batteries, J. Electrochem. Soc. 161 (5) (2014) A803–A813.

[59] A.I. Lurie, Nonlinear Theory of Elasticity, Nauka, Moscow (in Russian), 1980.

[60] A.I. Lurie, Nonlinear Theory of Elasticity, North Holland, Amsterdam, 1990.

[61] D.S. SIMULIA, ABAQUS 6.14 guides (2014).

[62] S.N. Atluri, G. Yagawa, T.A. Cruse, Computational Mechanics '95: Theory and Applications. Vol. I & II, Springer-Verlag, New York, 1995.

[63] N. Nguyen, A.M. Waas, Nonlinear, finite deformation, finite element analysis, Zeitschrift für angewandte Mathematik und Physik 67 (3) (2016) 35.